Extended hopanoid lipids promote bacterial motility, surface attachment, and root nodule development in the *Bradyrhizobium diazoefficiens-Aeschynomene afraspera* symbiosis

Belin, B.J.,[1] Tookmanian, E.T.,[1] de Anda, J.,[3] Wong, G. C. L.,[3] Newman, D.K.[1,2]

[1]Division of Biology & Bioengineering, [2]Division of Geological & Planetary Sciences, California Institute of Technology, Pasadena, CA.
[3]Department of Bioengineering, Department of Chemistry and Biochemistry, and California NanoSystems Institute, University of California Los Angeles, Los Angeles, CA 90095-1600, USA University of California Los Angeles, Los Angeles, CA.

Abstract

Hopanoids are steroid-like bacterial lipids that enhance membrane rigidity and promote bacterial growth under diverse stresses. Roughly 10% of bacteria contain genes involved in hopanoid biosynthesis, and these genes are particularly conserved in plant-associated organisms. We previously found that the extended class of hopanoids (C_{35}) in the nitrogen-fixing soil bacterium *Bradyrhizobium diazoefficiens* promotes its root nodule symbiosis with the tropical legume *Aeschynomene afraspera*. By quantitatively modeling root nodule development, we identify independent roles for hopanoids in the initiation of root nodule formation and in determining the rate of root nodule maturation. *In vitro* studies demonstrate that extended hopanoids support *B. diazoefficiens* motility and surface attachment, which may correlate with stable root colonization *in planta*. Confocal microscopy of maturing root nodules reveals that root nodules infected with extended hopanoid-deficient *B. diazoefficiens* contain unusually low densities of bacterial symbionts, indicating that extended hopanoids are necessary for persistent, high levels of host infection. This work identifies extended hopanoids as regulators of the efficiency of *Bradyrhizobia* nitrogen-fixing symbioses, agriculturally and economically significant associations with growing importance in a changing climate.

Introduction

Hopanoids are steroid-like lipids synthesized by metabolically and environmentally diverse bacteria. Studies in multiple organisms have shown that hopanoids support bacterial survival in response to stress, including growth under conditions of high osmolarity, low pH, elevated temperatures, detergents, and antibiotics (reviewed in ref. 1). It is thought that hopanoids primarily promote survival by rigidifying and decreasing the permeability of membranes,[2,3] providing a better barrier against external insults. Hopanoids may also directly regulate proteins, chemical signals, and other lipids in the membrane (as do eukaryotic sterols[4]), but such interactions are yet to be characterized.

Hopanoids consist of a 30-carbon pentacyclic core, generated by the squalene-hopene cyclase (*shc*) family of enzymes,[5,6] that can be modified to generate a medley of distinct molecules. The most common hopanoid modifications are methylation by the enzyme HpnP[7] and addition of a ribose-derived side chain by the enzyme HpnH (Fig. 1a)[8]. Downstream enzymes can further diversify side chains added by HpnH,[9] and the resulting molecules are known collectively as the C_{35} or extended hopanoids. Common extended hopanoid side chains include aminotriol-, polyol-, and adenosyl- moieties, although organism-specific side chains have also been observed. For example, the *Bradyrhizobiaceae* family of soil bacteria encode an extended hopanoid with a lipid A side chain, known as HoLA[10–12]. It is an open question whether HoLA and other specific extended hopanoids perform non-overlapping functions in cells, although evidence that methylated and extended hopanoids affect membrane biophysics and stress tolerance to differing degrees supports this notion (reviewed in ref. 1).

In the environment, hopanoid biosynthesis genes are enriched in plant-associated metagenomes,[13] and they are highly conserved in the plant growth-promoting *Bacilli*, *Nostoc* and *Anabaena* symbionts of various green plants, and *Frankia* and *Bradyrhizobia* nitrogen-fixing symbionts of legumes[14,15]. We previously found that hopanoids are required for optimal symbiosis of two strains of *Bradyrhizobia*, the photosynthetic *Bradyrhizobium* BTAi1 and the model *Bradyrhizobium diazoefficiens*, with members of the *Aeschynomene* genus of tropical legumes[10,11]. The symbiotic properties of *B. diazoefficiens* are of particular agricultural and economic significance because it natively forms symbioses with soybean crops[16]. In a *B. diazoefficiens-Aeschynomene afraspera* symbiosis model, we found that the bacterial extended hopanoids specifically are required for optimal rates of *in planta* nitrogen fixation[11].

Numerous processes in bacteria and plant hosts determine the rate of nitrogen fixation in legume-rhizobia symbioses. The most basic requirement is the inherent capacity of bacteria to perform the nitrogen fixation reaction, which demands a high uptake of various trace metals, rapid consumption of protons and ATP, and the absence of freely-diffusing oxygen. In *Frankia* legume symbionts, it has been suggested that hopanoids help to maintain a low-oxygen environment by limiting oxygen diffusion across membranes[17–19], although comparative measurements of free oxygen in wild type and hopanoid-deficient strains have not been performed.

Another determinant of root nodule nitrogen fixation levels is the efficiency of root nodule development, beginning with rhizobial colonization of the plant root surface. In *Aeschynomene* hosts root colonization occurs on plant root "cracks", breaks in the outer epidermal layers formed naturally by lateral root emergence[20]. *B. diazoefficiens* possesses two systems that guide motility towards these cracks, a constitutive subpolar flagellum and inducible lateral flagella[21], which appear to fill complementary roles. The subpolar flagellum primarily drives chemotaxis in open aquatic environments, whereas the lateral flagella promote motility on surfaces or in viscous fluids[22]; presumably these activities correspond to persistent, long-range movement towards hosts and clearing obstacles on the soil and root surface, respectively[23,24]. In *A. afraspera,* root surface colonization also requires bacterial Nod factors, immunosuppressant molecules that activate pro-symbiotic signaling[25].

After stable colonies are established at root cracks, rhizobial infections progress to the root interior. The cytological details of this process have been characterized for *A. afraspera* only in association with the *Bradyrhizobium* strain ORS285,[25] and in this context, rhizobia can be observed invading roots via thread-like patterns in the intercellular spaces of the inner epidermal and cortical cell layers. At the cortex, several host cells become intracellularly infected with bacteria. These infected cells appear to internalize the bacteria through narrow membrane invaginations, each enclosing multiple bacterial cells, that pinch off to form intracellular infection pockets[25]. In a few infected cells, these infection pockets presumably break down into symbiosomes, an organelle-like structure consisting of intracellular bacteria (now called "bacteroids") surrounded by a plant membrane, which is the basic nitrogen-fixing unit and defining feature of the root nodule.

Two developmental programs follow symbiosome formation in *A. afraspera*. In the first, infected host cells enter a proliferative state[25], forming the nodule primordium, and grow to form a large, spherical mass of infected cells known as the central infection zone. As the infection zone develops it is enveloped by epidermal tissue, and eventually, a vasculature system. This pathway for infection zone formations is unusual among legumes. More commonly, the nodule primordium arises from a meristem that is regulated independently and spatially separated from the bacterial invasion site; paradoxically, bacterial internalization in meristem-dependent nodules often inhibits, rather than stimulates, further host proliferation[26]. Another notable feature of *A. afraspera* is that two or more discrete infection zones may develop in the same nodule, resulting in a multi-lobed morphology. Each infection zone is thought to arise from a single infected cell, as co-inoculation of *A. afraspera* with a mixture of GFP- and mCherry-expressing *Bradyrhizobia* strains generally results in infection zones expressing only one fluorophore[25,27].

The second program initiated by symbiosome formation is the establishment of major genetic and chemical changes for bacteroids, including a sharp reduction in pH[28] and free oxygen levels[29] in the surrounding environment, high levels of bacteroid genome duplication, suppression of non-symbiotic genes, extreme changes in bacterial morphology, and a loss of bacteroid viability. These genetic changes are directed largely by antimicrobial NCR (nodule cysteine-rich) peptides produced by legume hosts (reviewed in 30). Mutant rhizobia with higher susceptibility to the NCR peptides *in vitro* tend to be ineffective symbionts that trigger plant defense reactions or early senescence of root nodules, a process in which the central nodule tissue is degraded and recycled by the host[31].

In this study, we sought to better understand how the extended hopanoids of *B. diazoefficiens* support nitrogen fixation in the *A. afraspera* root nodule symbiosis. We found that the lower nitrogen fixation of extended hopanoid mutants can be explained by a reduction in root nodule size and rhizobial occupancy, indicating that the underlying defect is primarily developmental rather than relating to per-bacteroid nitrogen fixation productivity. By novel application of a quantitative framework for modeling plant tissue growth using single-nodule tracking, we find that extended hopanoids support root nodule development through two independent pathways: by promoting bacterial motility towards and attachment to root surfaces and by maintaining normal host and symbiosome proliferation rates in the infection zone. In addition, our results reveal the dynamics of nodulation in *A. afraspera*, demonstrating that for these plants nodulation occurs in bursts separated by fixed intervals that do not depend on net fixed nitrogen

production across the root. We further suggest that nodule growth rates are key determinants of an *A. afraspera* nodule's nitrogen fixation output at maturity, in which growth rates may be "tuned" to stimulate proliferation in nodules with more effective symbionts.

Results

Loss of extended hopanoids results in reduced nodule size

Previously, we observed a symbiotic defect for a mutant lacking extended hopanoids (Δ*hpnH*) in the *B. diazoefficiens-Aeschynomene afraspera* symbiosis model[11]. To verify and better understand this defect, we inoculated *A. afraspera* plants with Δ*hpnH*, Δ*hpnP* (lacking 2-Me hopanoids), or wild-type *B. diazoefficiens*. At 24 days post-inoculation (dpi), plants inoculated with Δ*hpnH* were shorter than wild type-inoculated plants, although both strains produced equivalent numbers of nodules (Fig. 1b). Δ*hpnH*-inoculated plants also exhibited a roughly 50% decrease in the rate of reduction of acetylene gas (a proxy for nitrogen fixation) compared to wild type-inoculated plants at this time point (Fig. 1c). In contrast, the Δ*hpnP* mutant was similar to wild type (Fig. 1b-c). These results are consistent with our previous findings[11].

We initially hypothesized that the Δ*hpnH* defect in nitrogen fixation *in planta* occurs because of poor survival of the Δ*hpnH* mutant in hosts, given that *in vitro* the Δ*hpnH* strain is more susceptible to conditions mimicking the nodule environment (*e.g.* low pH, low oxygen, high osmolarity, and NCR peptides)[11]. To assess Δ*hpnH* viability within *A. afraspera* nodules, we performed morphological analyses of nodule semi-thin sections using confocal fluorescent microscopy. Hand-sectioned nodule slices (of roughly 200-500 μm thickness) were stained with a bacterial live:dead kit, consisting of the SYTO9 DNA dye, which is cell-permeable and labels all cells, and propidium iodide (PI), a dye that uniquely labels cells with compromised membranes, which are generally non-viable. Contrary to our expectations, we did not observe an increase in PI staining in nodules containing Δ*hpnH* (Fig. 1d; Fig. 1-S1,1-S2). Signatures of plant defense reactions, which previously were associated with Δ*hpnH*[11], were also rare, occurring prominently in only ~1.5% (1/67) of nodules (Fig. 1-S2).

The most apparent difference in the morphology of Δ*hpnH* nodules compared to wild type was the presence of relatively small nodules (Fig. 1-S1,1-S2). To determine whether lower nodule size could explain reduced nitrogen fixation in Δ*hpnH*-inoculated plants, we repeated acetylene reduction assays for wild-type- and Δ*hpnH*-inoculated plants, harvested their nodules, and calculated the total nodule dry mass for each plant at 24 dpi. We found a decrease in the nodule dry mass per plant for Δ*hpnH*-inoculated plants that is commensurate with the decrease in acetylene reduction rates (Fig. 1e). After normalization by nodule dry mass, no significant difference could be observed in acetylene reduction between the wild-type- and Δ*hpnH*-inoculated plants (Fig. 1e). This suggests the *in planta* nitrogen fixation defect of Δ*hpnH* at 24 dpi can be explained by smaller average nodule sizes. It also rules out the possibility that nitrogenase functions ineffectively in the absence of extended hopanoids due to inactivation by oxygen, as has been suggested in *Frankia*[17–19], as the per-mg nitrogen fixation rates are unaffected in Δ*hpnH*.

ΔhpnH nodules are more variable in size than wild-type nodules

Curious about the origin of the smaller Δ*hpnH* nodule sizes, we devised three *a priori* hypotheses for how small nodules could arise: first, that Δ*hpnH* nodule growth is terminated prematurely; second, that Δ*hpnH* nodules grow at a slower rate; and third, that the initiation of Δ*hpnH* nodules is delayed. Of these scenarios, the first possibility is unique in that Δ*hpnH* nodules would be *necessarily* smaller than wild type; in other words, Δ*hpnH* nodules could not "catch up" to wild type given additional time. To test this possibility, we measured acetylene reduction per plant across an extended 40 dpi period, and we observed that the differences in both acetylene reduction rates and nodule dry masses between wild type and Δ*hpnH* steadily decreased with time (Fig. 2a-b). By 40 dpi the overall symbiotic efficiencies of wild type and Δ*hpnH* per plant were indistinguishable, in terms of the plants' qualitative appearance (Fig. 2c,d) as well as their average shoot heights and acetylene reduction rates (Fig. 2-S1). Total nodule counts per plant also did not differ between wild type and Δ*hpnH* at 40 dpi, indicating that the increase in total nodule mass reflects growing nodules rather than more frequent nodulation (Fig. 2-S1).

These total dry mass measurements appeared consistent with Δ*hpnH* nodules "catching up" to wild type, so we sought to independently verify this interpretation by measuring the radii of individual nodules on ten plants for each strain at 40 dpi (Fig. 2e,f). From these data we determined that although

average nodule sizes (and, by extension, the total nodule mass) did become similar between strains by this time point (0.73 vs. 0.88 mm average radii), their underlying distributions were markedly distinct. Wild-type nodule radii appear to form a roughly normal distribution, whereas the Δ*hpnH* nodule radius distribution is bimodal, consisting of a subpopulation of small nodules with small radii (<0.5 mm) that are rarely observed in wild type, as well as a second, larger subpopulation that has a similar median radius as wild type but is skewed towards larger radii (>1.5mm). These data demonstrate that the small-nodule phenotype of Δ*hpnH* persists throughout a 40 dpi time course, but is compensated by greater size heterogeneity, in which a handful of "mega" nodules offset smaller nodules over time.

ΔhpnH *nodule size heterogeneity reflects variable nodule growth rates*

The static measurements described above were insufficient to evaluate our hypothesis that Δ*hpnH* nodule growth is aborted, because we could not infer from these assays whether the small nodules observed at 24 (Fig. 1) and 40 (Fig. 2) dpi represent the same population, or whether they simply began growing at different times. To better evaluate the possible mechanisms of the Δ*hpnH* nodule size defect, we studied the kinetics of single nodule development. Beginning one week after inoculation of *A. afraspera* plants with either wild type or Δ*hpnH*, we collected images of entire plant roots every 3-5 days up to ~40 days post-inoculation (Fig. 3-S1, 3-S2). From these images, we identified nodules that were clearly visible (*e.g.* not obscured by lateral roots or more recently emerged nodules) in at least five time points (Fig. 3a) and measured their radii. We then calculated nodule volumes by approximating nodules as spheres and plotted the volume of the tracked nodules over time. While we again observed that many Δ*hpnH* nodules were smaller at 40 dpi than any of the wild type nodules, we also found that nodule growth was highly variable both within and between strains (Fig. 3b,c).

To describe this heterogeneity, we employed a simple framework for quantifying nodule development. We describe nodule growth by the following variables: the time (t_i) of the initial intracellular infection event and the volume of the nascent nodule (V_i), equivalent to the volume of one infected *A. afraspera* cortical cell; the time (t_{min}) and volume (V_{min}) at which a clearly visible, spherical nodule has developed; the rate of growth of a nodule once it has become visible (dV/dt); and the time (t_{max}) and volume (V_{max}) of a nodule when its growth has stopped (Fig. 3d). To calculate these variables, we fit each nodule's growth over time to three different growth models: exponential, quadratic, and a generalized logistic (*e.g.* sigmoidal) equation commonly used for plant growth[32,33] (see Methods for complete details). Sigmoidal models generally provided the best fit to the experimental data, so these models were used for growth parameter calculation (Fig. 3e; Fig. 3-S3, 3-S4).

The growth rates of Δ*hpnH* nodules were lower on average than wild-type nodules (Fig. 3f), with roughly a third of tracked nodules exhibiting growth rates lower than observed for wild type by 40 dpi (<0.1 mm^3/dpi). We noted that this was the same fraction of nodules as in the subpopulation of nodules with smaller-than wild type radii at 40 dpi (Fig. 2e; Fig. 3g), and indeed, the subpopulation of nodules with lower-than-wild-type growth rates and small nodule sizes are the same (Fig. 3h). Additionally, we found that the growth rate of a nodule and its maximum size are positively linearly correlated for both strains, with Pearson coefficients of ~0.64 (p<10^{-9}) for wild type and ~0.75 (p<10^{-15}) for Δ*hpnH*. We interpret these data to suggest that host proliferation is slower in a subset of nodules infected with Δ*hpnH*, and that this at least partially accounts for the low final volume of these nodules.

We also noted that the Δ*hpnH* nodule sizes at 40 dpi differed between these single-nodule volume measurements (Fig. 3g) and our previous 40 dpi end-point measurements of nodule radii (Fig. 2e), in that we did not observe larger-than-wild-type "mega" nodules in the single-nodule dataset. This discrepancy likely reflects the smaller sample size in our single-nodule tracking experiments (84 compared to 268 end-point nodules), and the low frequency of "mega" nodule formation. To verify this, we selected 10,000 random subsets of 84 nodules from the 268 Δ*hpnH* nodules shown in Figure 2e, converted the nodule radii to volumes, and found that there is no statistically significant difference (p<0.05) between a random subset of Fig. 2e and the Δ*hpnH* single-nodule tracking data in ~92% (9184/10000) of cases. Thus the differences in nodule size distributions in Figure 3g and Figure 2e are consistent with sampling error.

We also used nodule growth fitting to test our hypothesis that the growth period is shorter for Δ*hpnH* nodules compared to wild type – *e.g.* that growth stops prematurely. We estimated the window of maximum growth as the time required for a nodule to increase from 10% to 90% of its final volume. Neither the time at which a nodule reaches 90% of its maximum volume, t_{max}, nor the window of maximum growth differs significantly between Δ*hpnH* and wild type (Fig. 3-S5a,b). The window of

maximum growth for each nodule is also uncorrelated with their final volume or growth rate, indicating that small nodules are not prematurely aborted; rather, their growth periods are similar to larger nodules (Fig. 3-S6a-d).

To better understand the subpopulation of small, slow-growing $\Delta hpnH$ nodules, we sectioned nodules from $\Delta hpnH$-inoculated plants at 40 dpi and separated the small (<0.5 mm radius) subpopulation of nodules from all others (>0.5 mm radius). We stained sections with SYTO9, PI and Calcofluor and imaged the sections with confocal microscopy. We found that while most small $\Delta hpnH$ nodules contained a single, continuous infection zone, a large fraction were un- or under-infected with bacteria, often exhibiting disorganized central infection zones (~37%; 28/75) (Fig. 4a; Fig. 4-S1). Of the fully infected small $\Delta hpnH$ nodules, some contained primarily PI-stained, likely dead bacterial cells (~25%; 12/47) (Fig. 4a; Fig. 4-S1). Similarly high proportions of under-infected nodules or nodules primarily occupied with membrane-compromised bacteria did not occur in larger $\Delta hpnH$ nodules harvested at the same time point; however, we did notice that many of these nodules contained noticeably fragmented infection zones (Fig. 4b; Fig. 4-S2).

We also compared the subpopulation of small $\Delta hpnH$ nodules at 40 dpi to two wild-type nodule populations: similarly small nodules harvested at 10 and 25 dpi (Fig. 4a; Fig 4-S3; Fig. 4-S4), and nodules harvested at the same 40 dpi time point (Fig. 4b; Fig. 4-S5). Again, we found that higher proportions of under-infected nodules and nodules containing primarily membrane-compromised bacteria were unique to the $\Delta hpnH$ small-nodule subset. It is interesting that these phenotypes were not apparent for $\Delta hpnH$ nodules in the previously analyzed 24 dpi time point (Fig. 1-S1), in which nodules that are under-infected or primarily occupied by dead bacteroids are rare. It is possible we did not capture these phenotypes because they occur infrequently in the overall nodule population; infection zones with primarily dead bacteroids occur in only 12/75 small $\Delta hpnH$ nodules in Fig. 4-S1, and small (<0.5 mm radius) nodules themselves make up only a third of all $\Delta hpnH$ nodules at 40 dpi. An alternate conclusion from these data is that poor $\Delta hpnH$ survival or infection density is only apparent at later stages in development, indicating inherently poor persistence of $\Delta hpnH$ within host cells and/or premature nodule senescence.

ΔhpnH is delayed in early plant-symbiont association

Our final hypothesis for the origin of small nodules, that the onset of nodule growth is delayed, proved more difficult to address. The "true" beginning of nodule formation is the time when the first *A. afraspera* cortical cell is infected, t_i (Fig. 3d). However, this initial infection event is not visible at the root surface, and it is difficult to extrapolate from sigmoidal models in which the growth curves approach the initial volume $V_i \sim 0$ mm^3 asymptotically. As a proxy for t_i, we defined three alternate t_{min} as the times at which nodules reached three arbitrarily small volumes: $V = 0.05$ mm^3, $V = 0.1$ mm^3, and $V = 0.2$ mm^3. When t_{min} is defined by $V = 0.05$ mm^3 or 0.1 mm^3, t_{min} could not be accurately calculated for all nodules, as the sigmoidal models sometimes predicted $t_{min} < 0$ (an impossible value) (Fig. 3-S5c). These nodule volumes are also too small to be seen on the root surface, and we had no experimental means to determine the accuracy of the calculations in this low-volume regime. When t_{min} is defined by $V = 0.2$ mm^3 (the smallest nodule volume that we could identify in our single-nodule tracking assays), there is a small but statistically significant increase for $\Delta hpnH$ relative to wild type (Fig. 3-S5c). To independently verify this delay in visible nodule appearance, we inspected the roots of 20 wild type- and 20 $\Delta hpnH$-inoculated plants over 40 dpi and recorded the number of visible nodules per plant each day. We found a more even distribution of observed t_{min} for $\Delta hpnH$ relative to wild type, with a 1-3 day shift in the most frequent dpi. Surprisingly, we also found that the formation of new nodules is periodic, with a new "burst" of nodules emerging roughly every 18 days (Fig. 3i). This periodicity of nodule emergence appears to be similar between strains.

While the slight t_{min} delay for $\Delta hpnH$ is consistent with longer times required to initiate the symbiosis (*e.g.* root surface colonization, invasion of the root epidermis and cortex, and intracellular uptake), it is also possible that a delay in t_{min} simply reflects a lower rate of nodule growth immediately after the first host cell is intracellularly infected. To address this, we compared the calculated value of t_{min} (defined by $V = 0.2$ mm^3) to the maximum growth rates and volumes for each nodule (Fig. 3-S6e,f). We did not find that the subpopulation of nodules with lower growth rates and final volumes than wild type was more likely to have a later t_{min}, supporting the interpretation that the delay in t_{min} of $\Delta hpnH$ could be due to a separate initiation defect, although it is also possible that the growth rates of emergent nodules and nascent nodule primordia are not strictly related. Interestingly, t_{min} is also not correlated with the period in which maximum nodule growth occurs, such that later-emerging nodules have similar periods of

growth as nodules formed within a few dpi (Fig. 3-S6g,h). This indicates that although the appearance of new nodules is restricted to narrow, periodic time frames (Fig. 3i), once a nodule has entered its maximum growth phase, its continued growth is comparatively unconstrained.

To further verify the slight delay in the initiation of the symbiosis for Δ*hpnH* relative to wild type, we performed competition assays using a standard fluorescence labeling approach. We first generated Δ*hpnH* and wild-type strains expressing chromosomally-integrated fluorescent proteins, and then we co-inoculated *A. afraspera* with different ratios of these two strains. As control experiments, we also co-inoculated each tagged strain with its untagged counterpart, in order to determine the effect of fluorescent protein overexpression on each strain's competitiveness. After >40 dpi we measured the size of nodules on plants inoculated with each strain combination and ratio, then sectioned and fixed nodules for imaging. Although we expected each nodule to contain a clonal population based on previous work[25,27], the majority of nodules appeared to contain a mixture of both strains (Fig. 5a; Fig. 5-S1-5). We instead quantified the relative abundance of each strain in each nodule by fluorescence imaging; in our control experiments, in which only one fluorophore-expressing strain was present, a DNA dye (either SYTO9 for mCherry-expressing bacteria or PI, which stains all cells in fixed samples, for GFP-expressing bacteria) was used to label all bacteria.

Both WT-YFP and Δ*hpnH*-mCherry were significantly out-competed by their corresponding untagged strains, with higher proportions of tagged strains correlating with lower bacterial DNA abundance and smaller nodule and/or infection zone sizes (Fig. 4b-c; Fig. 5-S7,8). Additionally, plants co-inoculated with untagged-Δ*hpnH* and Δ*hpnH*-mCherry were significantly shorter than plants inoculated with untagged-Δ*hpnH* only, suggesting Δ*hpnH*-mCherry is symbiotically defective (Fig. 5-S6). These effects of fluorophore overexpression made it difficult to interpret our WT-YFP and Δ*hpnH*-mCherry competition data (Fig. 5-S9), so we developed an alternative, antibiotics-based method to study the timing of early symbiotic initiation.

First we sought antibiotics that were effective against *B. diazoefficiens* but would minimally affect *A. afraspera* growth. We selected three antibiotics (100 μg/ml streptomycin, 100 μg/ml kanamycin, and 20 μg/ml tetracycline) and treated non-inoculated plants with these antibiotics for two weeks, alone and in combination. After this treatment, we found that neither kanamycin nor streptomycin, nor the combination of the two, significantly affected plant appearance, shoot height, or root and shoot dry masses compared to untreated controls (Fig. 5-S10). Plants treated with tetracycline were noticeably more yellow in color, indicating chlorosis, and the roots and plant medium became brown; these plants also had lower shoot and root dry masses than untreated plants (Fig. 5-S10).

Next, because the Δ*hpnH* strain is more sensitive to antibiotics than wild type[11], we tested various concentrations of the non-plant-perturbing antibiotics streptomycin and kanamycin to identify concentrations that would result in the same rates of cell death for both strains. We inoculated plant growth media with wild type or Δ*hpnH* to the same concentrations and under the same environmental conditions as in plant inoculation experiments. The wild-type culture was supplemented with 100 μg/ml streptomycin plus 100 μg/ml kanamycin, and Δ*hpnH* cultures were supplemented with decreasing concentrations of these antibiotics: 75, 50 and 25 μg/mL each. Samples of the cultures were then collected, serially diluted and added to PSY plates to estimate colony-forming units (cfus) per mL over time. At 50 μg/mL kanamycin plus 50 μg/mL streptomycin, the rate of decrease in cfus/mL for Δ*hpnH* was equivalent to that of wild type treated with 100 μg/ml kanamycin plus streptomycin (Fig. 5d).

Finally, we inoculated 40 plants each with wild type or Δ*hpnH* and added streptomycin or kanamycin to 100 μg/mL each or 50 μg/mL each, respectively, at various points post-inoculation. After 40 days we counted the number of nodules per plant, and found that antibiotics were able to block nodule formation over a ~50% longer window in Δ*hpnH* compared to wild type (Fig. 5e). The decrease in nodules formed at different antibiotic treatment time points was also evident in the overall appearance of the plants (Fig. 5f). These results suggest that Δ*hpnH* requires more time on average to reach the intracellular stage of the symbiosis, at which point we presume that the bacteria are protected from antibiotic by the host cells. These data are consistent with Δ*hpnH* requiring more time to colonize the root surface, invade the root epidermis, and/or be internalized by host cells.

Extended hopanoids support surface attachment and motility

Because we found that expression of genetic tags in wild type and Δ*hpnH* perturbed their symbiosis with *A. afraspera*, and therefore we could not confidently track these strains *in planta*, we used an *in vitro* approach to study two steps in the initiation of the symbiosis: (1) bacterial motility toward or

along the *A. afraspera* root, and (2) stable attachment of bacteria to the root surface[20]. To determine whether Δ*hpnH* is less motile than wild type, we inoculated low-agar, PSY plates with Δ*hpnH* or wild type and measured the rate of zone of swimming over time. We observed that diameter of motility was reduced in Δ*hpnH* compared to wild type (Fig. 6a-b), consistent with a swimming motility defect; however, because we have previously shown that Δ*hpnH* grows more slowly in this medium than wild type[11], we could not rule out the possibility that slower zone expansion simply reflects a longer doubling time.

To investigate the nature of the plate motility defect, we studied the motility of single *B. diazoefficiens* cells. We inoculated cells that have been incubated in PSY liquid medium into a glass bottom steril flow cell with 100μL of each strain and recorded the trajectories of single cells near the glass surface at 5 ms time resolution. The cells were tracked using an in-house tracking software in MATLAB,[34] in which actively swimming cells are defined as having super-diffusive motion and a trajectory radius of gyration greater than 2.5 μm, and we calculated mean swimming speeds for each cell using a moving window average over the cell's full trajectory (see Methods for details). In agreement with our low-agar swimming plates, we found a significantly lower (p < 0.0001) fraction of motile cells for Δ*hpnH*, $N_{\Delta hpnH}$ = 65 ± 29, compared to wild type, N_{wt} = 368 ± 60, in PSY medium (Fig. 6c), although the average mean-speed among motile cells were similar between strains, $<V>_{\Delta hpnH}$ = 24.83 ± 7.0 μm/sec and $<V>_{wt}$ = 22.75 ± 6.7 μm/sec (Fig. 6d). Because the composition of PSY differs greatly from that of the plant growth medium (BNM), we repeated these assays in BNM supplemented with arabinose. Under this condition, we again observed a lower fraction of motile Δ*hpnH* cells than wild type, ($N_{\Delta hpnH}$ = 54 ± 59, N_{wt} = 450 ± 310) (Fig. 6e), with similar mean speeds between strains and across media conditions (Fig. 6d,f). These results are consistent with a delay in the initiation of the Δ*hpnH* symbiosis with *A. afraspera* due to a lower occurrence of motile bacterial cells, indicating that the effect of extended hopanoids is likely regulatory and upstream of the workings of the flagellum.

We next tested the surface attachment capabilities of Δ*hpnH* and wild type by incubating dense bacterial cultures on glass coverslips and quantifying the fraction of the surface covered with stably adhered cells after two hours. In PSY medium, both strains adhered poorly, and there was no significant difference in their attachment efficiencies (Fig 6g; Fig. 6-S1). In BNM supplemented with arabinose, both strains adhered to glass better than in PSY, and Δ*hpnH* attachment levels were significantly lower than wild type (Fig. 6g; Fig. 6-S1). The origin of the differences in surface attachment between PSY and BNM is unclear. While this result may indicate that the surface attachment machinery of *B. diazoefficiens* functions better in BNM, we cannot exclude the interpretation that because PSY is more rich than BNM, peptides and other components of PSY are more likely to interact with the glass surface to occlude or disfavor bacterial attachment. Regardless, the lower adherence of Δ*hpnH* in BNM data suggest that Δ*hpnH* may adhere to the *A. afraspera* root surface less efficiently than wild type, and that this also may contribute to the delay in the initiation of the symbiosis.

Discussion

Hopanoids are well-established mediators of bacterial survival under stress, and previously we showed that the capacity for hopanoid production is enriched in plant-associated environments[13] and required for optimal *Bradyrhizobia-Aeschynomene* spp. symbioses[10,11]. Here we performed a detailed, quantitative evaluation of the extended hopanoids' roles in the *Bradyrhizobium diazoefficiens-Aeschynomene afraspera* symbiosis. Our results provide evidence that extended hopanoids' effects are pleiotropic and span the stages of root nodule biogenesis. We identify specific extended-hopanoid dependent processes that will provide a foundation for more detailed mechanistic work (Fig. 7). Our description of the kinetics of nodule growth in *A. afraspera*, both for single nodules and across the root system, more generally suggests new hypotheses about the cell and developmental biology of nodule formation in this organism.

By tracking the development of individual root nodules, we found that the initial emergence of root nodules is delayed in plants inoculated with extended hopanoid mutants. *In vitro*, extended hopanoids appear to support both the efficiency of surface attachment and the proportion of motile cells in plant growth medium, suggesting that delayed root nodule emergence may result from fewer cells swimming and attaching to the root surface in the initial bacteria-host contact (Fig. 7a-b). At later stages in root nodule development, roughly a third of nodules infected with extended hopanoid mutants grow at slower rates than with wild type and consequently exhibit low volumes when fully mature. Many of these small nodules contain reduced densities of symbionts throughout their infection zones; extended hopanoid mutant nodules with wild-type nodule volumes can also have lower symbiont loads, due to infection zone

fragmentation. The origin of this under-infection phenotype is unclear from our experiments. One explanation is that host cells in the nodule primordium either internalize fewer cells from the extracellular environment, or that primordial symbiosomes duplicate or are segregated less effectively, and this phenotype is simply propagated as nodules develop (Fig. 7d). Alternatively, low symbiont densities may reflect symbiont degradation in a previously fully-infected nodule (Fig. 7e).

What mechanisms might underpin these extended hopanoid mutant phenotypes? Through a biophysical lens, the effects of extended hopanoid loss in the *B. diazoefficiens-A. afraspera* symbiosis could be viewed purely as consequences of less rigid *B. diazoefficiens* membranes. The fraction of motile cells in *E. coli* populations has been suggested to be sensitive to changes to the mechanical properties of the outer membrane[35], and membrane-based mechanotransduction is required by diverse bacteria to stimulate extracellular matrix production and cement their attachment to surfaces[36,37]. Subsequent progression of bacteria into the root interior through small (micron- to submicron-diameter) channels may also be hindered by a less rigid *B. diazoefficiens* membrane, as growth rates under similarly confined spaces *in vitro* have been shown to be positively correlated with membrane rigidity in *E. coli* and *B. subtilis* models[38,39]. Though not much is known about the mechanical requirements of formation and propagation of the symbiosome, bacterial membrane rigidity may be relevant in this context as well. For example, the maintenance of single-bacteroid-containing symbiosomes within host cells (presumably requiring coordination of bacteroid division with division of the surrounding host-derived membrane) implies a mechanical linkage between the bacteroid and peribacteroid membranes, which may be sensitive to changes in bacteroid membrane rigidity. NCR peptide-directed reprogramming of bacteroids could also be less effective in *B. diazoefficiens* with less rigid membranes, increasing bacteroid permeability to peptides or peptide-induced bacteroid lysis. While intriguing, these mechanics-based roles for extended hopanoids are difficult to verify given how little information is available on the biophysical aspects of legume-microbe interactions. Future work in this area would enrich our understanding of how intracellular bacterial infections operate in native multicellular hosts.

Other potential extended hopanoid-mediated effects on the symbiosis include regulation of membrane-based processes, such as motility, oxidative phosphorylation, the early legume-rhizobia dialogue or transport across the symbiosome membranes. Specifically, the loss of HoLA from the outer membrane in the *B. diazoefficiens* ΔhpnH mutant is likely to disrupt processes involving lipid A, which has previously been shown to enhance bacterial fitness in *A. afraspera* hosts[40]. Identifying the enzyme(s) responsible for the attachment of hopanoids to lipid A will be necessary to determine how much HoLA contributes to the ΔhpnH phenotypes we observed in this work, as well as the universality of these phenotypes to other host-bacteria interactions. While many hopanoid-producing bacteria are host-associated, so far HoLA has only been found in the *Bradyrhizobiaceae*.

Regardless of the underlying mechanisms for extended hopanoids, it is curious that their absence is not a death knell for the *B. diazoefficiens-A. afraspera* symbiosis at any stage. In our *in vitro* studies, although fewer motile cells were present in the extended hopanoid mutants, mean speeds among motile ΔhpnH cells were indistinguishable from wild type. While we cannot rule out more subtle defects in the direction of the movement or in chemotaxis, the identical mean speeds suggest that once motility of ΔhpnH cells is induced, their motility systems function properly. Similarly *in planta*, ΔhpnH nodules developing at wild-type rates and reaching average wild-type volumes did occur – and, in the case of "mega" nodules, some exceeded their wild-type counterparts. Why do ΔhpnH populations form two distinct populations (wild-type-like or defective) rather than falling on a continuous distribution of behavior? Bimodality in a population can reflect a switch-like, or threshold-based, regulation, and perhaps in the ΔhpnH strain, a fraction of cells cannot support levels of signaling or biochemical events above the appropriate threshold for proper function. Populations within ΔhpnH also may differ in the extent to which extended hopanoid loss is compensated. In *Methylobacterium extorquens* and *Rhodopseudomonas palustris*[41,42], hopanoid loss results in upregulation of other membrane-rigidifying lipids including carotenoids and cardiolipins, and in other plant-microbe systems, lipid exchange between hosts and microbes has been observed[43], suggesting that ΔhpnH mutant success at a given nodulation site may relate to the local availability of exogenous plant steroids or structurally similar metabolites.

Beyond hopanoids, our results provide insight into the developmental control of nodule formation by *A. afraspera* hosts. Although the time of emergence, growth rate and window of growth of any specific nodule appears to be stochastic, the extent to which nodulation is permitted across the entire root system is tightly determined. Host control of nodule numbers, known as the autoregulation of nodulation (AON), is a well-established phenomenon[44], and a new, expanded model of AON derived from studies of *Lotus*

japonicum has recently been published[45]. In this model, the root-specific TOO MUCH LOVE (TML) protein is a key negative regulator of nodule formation. In the absence of rhizobia, a microRNA (miR2111) produced in plant leaves translocates to roots to suppress TML, poising uninfected plants in a nodulation-susceptible ("ON") state. When rhizobia begin to infect the plants, a negative feedback loop is initiated, beginning with the local production of CLE-family peptides. These CLE peptides then translocate to the shoot and activate a receptor protein at the shoot apex known as HAR1. HAR1-mediated signaling blocks the miR2111 shoot-root translocation, de-repressing TML to create a nodulation-resistant ("OFF") state.

The general features of this AON pathway are conserved across legumes (reviewed in [44]), and although AON has not been specifically investigated in *A. afraspera*, our results suggest a similar mechanism is at play. Our observation that the wild-type *B. diazoefficiens*-*A. afraspera* symbiosis is characterized by an initial 2-3 day burst of nodulation followed by a sharp drop-off is consistent with an initial "ON" state that is inhibited by a negative feedback loop with a several-day activation time. What is most striking about nodule formation in *A. afraspera* is that nodulation-susceptible "ON" states appear to be reactivated at fixed 18-day intervals, and that re-activation is unrelated to systemic nitrogen fixation efficiency: at the end of the first 18 dpi cycle, Δ*hpnH* nodules fix considerably less nitrogen than wild type, yet the timing and distribution of nodulation in the second cycle is unchanged. This both suggests that there is a fixed oscillation between nodulation-susceptible and nodulation-resistant states in *A. afraspera*, and that the timing of the oscillation is determined by the dynamics of the underlying regulatory mechanisms (*e.g.* the rates of synthesis, activation/inhibition, and translocation of specific regulatory molecules). Thus, we predict that a systems-level analysis of regulatory factor dynamics will be key to elucidating the nodulation re-activation pathway, as will a more detailed analysis of nodulation timing in other, model legumes. Specifically, it will be interesting to determine whether re-activation occurs simply by dampening of the negative feedback pathway as inhibitory molecules reach the end of their lifetimes, or if it involves an additional positive feedback mechanism that simply requires a longer activation time.

Since the systemic control of nodulation is insensitive to nitrogen fixation, it is possible that *A. afrapera* plants maximize overall nitrogen fixation through the local regulation of nodule organogenesis. It is already known that nitrogen-based signaling can locally regulate nodule formation in other legume hosts (reviewed in [44]), albeit in the context of nodule growth inhibition by increased soil nitrogen availability. We have found that the key variable that determines the final size of a nodule (and thus it potential for symbiotic productivity) is the rate of nodule growth and, given that rates of growth are lower in the less-productive Δ*hpnH* strain than wild-type, this could be coupled to the nodule's fixed nitrogen output. Alternately, nodule growth rates may relate to the density and survival of symbionts present, perhaps by indirect sensing of bacteroid-produced signals. An intriguing possibility is that bacteroids secrete mitogenic compounds, such as phytohormones, to directly influence host cell division rates. *B. diazoefficiens* has been shown to synthesize the majority of known phytohormones in pure culture[46], and in *Frankia* symbionts, extended hopanoid levels may be correlated with amount of the auxin phytohormome phenyl-acetic acid (PAA)[47]. It has also been shown that *B.* ORS285 mutants that cannot produce cytokinin phytohormones exhibit slower nodulation kinetics and smaller nodule sizes in *Aeschynomene indica* hosts[48]. The full extent to which primordia and infection zone growth are dependent on bacteroid-secreted mitogens or nitrogen fixation productivity, and through what mechanisms, will be an active area of future research.

On a technical level, our results underscore the importance of identifying the most informative, least perturbing tools for interrogating legume-microbe symbiosis. Employing quantitative single-nodule and single-cell approaches rather than bulk measurements were essential for uncovering the diverse phenotypes of the *B. diazoefficiens* extended hopanoid mutants and yielded unexpected information on regulation of nodule development by *A. afraspera*. We have also shown the limitations of introducing overexpressed genetic tags into bacteria. While use of these tags has undoubtedly enhanced our understanding of legume-microbe symbiosis[49], they may not fully capture the behavior of native organisms, and in this work we provide a model for evaluating the extent of these genetic tags' effects. Additionally, our work is one of many to emphasize the importance of appropriate culture models for mimicking the host environment, as the Δ*hpnH* surface attachment defect was observed in plant growth medium but not in a standard richer medium. Recent work has suggested that culturing rhizobia in the latter is correlated with an increase in mutations of symbiosis-associated genes[50], raising questions about the utility of rich medium cultures in symbiosis work overall. A more detailed analysis of the host environment, including the full milieu of root exudates[51], available carbon sources[52] and trace metals specific to each legume, will improve *in vitro* models of legume-bacteria interactions.

Finally, beyond opening up future work on the mechanism of hopanoids in motility and attachment, this work highlights aspects of the development of *A. afraspera* symbioses most in need of more detailed analysis. Key questions raised in this study include how relevant the biophysical environment of the root invasion is for the mode and the efficiency of progressive bacterial invasion; how is a high density of symbiosomes established and maintained within infected nodule cells; what factors regulate the mitotic index of a nodule, and how dynamic are these indices; and how the answers to all of these questions change in the presence of competition between multiple strains with different symbiotic nitrogen-fixation capacities. Addressing these questions in the *Aeschynomene-Bradyrhizobia* symbiosis will expand our knowledge of the diversity of approaches to establishing persistent, intracellular infections, and perhaps provide a better "blueprint" for engineering novel beneficial plant-microbe associations. These future studies may also prove to be ecologically significant, as African *Aeschynomene* spp. are native to regions with the world's poorest food security and nitrogen fertilizer accessibility and thus in greatest need of better symbiotic nitrogen fixation[53], and *Bradyrhizobia* are dominant in harsh, warm soils predicted to be more prevalent in a changing global climate[54].

Methods

B. diazoefficiens *culture and strain generation*

B. diazoefficiens hopanoid biosynthesis mutants were generated previously[11]. For construction of YFP- and mCherry-expressing strains, fluorophore expression vectors pRJPaph-YFP and pRJPaph-mCherry[27] were provided as a gift from Prof. Dr. Hans-Martin Fischer (ETH Zurich). These vectors were introduced into *B. diazoefficiens* by conjugation with the β2155 DAP auxotroph strain of *E.coli*, using the following protocol: *B. diazoefficiens* wild type and Δ*hpnH* were grown in 5 mL PSY medium[55] at 30°C and 250 rpm to an OD_{600} of ~1.0 (wild type) or of 0.5-0.8 (Δ*hpnH*). β2155 strains carrying pRJPaph vectors were grown to an OD_{600} of 0.5-0.8 in 5 mL LB supplemented with 10 µg/mL tetracycline and 300 µm DAP at 37°C and 250 rpm. Both *B. diazoefficiens* and β2155 donor cultures were pelleted at 3250 x g for 30 minutes, washed three times in 0.9% sterile saline, and resuspended in 0.9% sterile saline to a final OD_{600} of 1.0. *B. diazoefficiens* strains and β2155 donor cells were combined at a 4:1 ratio, respectively, and mixed by repeated pipetting. Aliquots (50 µl) of these 4:1 mixtures were dropped to PSY plates supplemented with 300 µm DAP, dried in a biosafety cabinet, and incubated for 48 hours at 30°C. Conjugation pastes were then removed from plates and resuspended in 5 mL sterile saline, pelleted at 3250 x g for 30 minutes and washed twice, in order to remove residual DAP. Washed cells were pelleted a final time and resuspended to 200 µl in 0.9% sterile saline and plated onto PSY plates supplemented with 20 µg/mL (wild type) or 10 µg/mL (Δ*hpnH*) tetracycline. Colonies appeared after 7-10 days (wild type) or 10-14 days (Δ*hpnH*) and were streaked onto fresh PSY/tetracycline plates, then screened for fluorescence using a Lumascope 720 fluorescent microscope (Etaluma). Fluorescent colonies were then sequenced to verify insertion of the pRJPaph vectors into the *scoI* locus.

A. afraspera *cultivation and inoculation with* B. diazoefficiens

A. afraspera seeds were obtained as a gift from the laboratory of Dr. Eric Giraud (LSTM/Cirad, Montpelier, France). Seeds were sterilized and scarified by incubation in 95% sulfuric acid at RT for 45 minutes, followed by 5 washes in sterile-filtered nanopure water and a second incubation in 95% ethanol for 5 minutes at RT. After ethanol treatment seeds were washed 5X and incubated overnight in sterile-filtered nanopure water. Seeds were then transferred to freshly poured water/agar plates using sterile, single-use forceps in a biosafety cabinet, and germinated for 24-72 hours in the dark at 28-32°C.

Seedlings were then placed in clear glass test tubes containing 100 mL of sterile, nitrogen-free Buffered Nodulation Medium (BNM)[56] and grown for 7-10 days in plant growth chambers (Percival) under the following settings: 28°C, 80-90% humidity, and 16 hour photoperiod under photosynthetic light bulbs (General Electric) emitting ~4000 lumens/ft^2. In parallel, *B. diazoefficiens* strains were grown in 5-10 mL PSY liquid culture at 30°C and 250 rpm to stationary phase (OD_{600} > 1.4). Stationary phase cultures were diluted into PSY one day prior to plant inoculation to reach an OD_{600} of ~0.8 at the time of inoculation. OD_{600} ~ 0.8 cultures were pelleted at 3250 x g for 30 minutes at RT, washed once in PSY, then resuspended in PSY to a final OD_{600} of 1.0. Resuspended *B. diazoefficiens* cultures were directly inoculated into the plant medium in a sterile biosafety cabinet; 1 mL of OD_{600}=1.0 culture was added per plant. Inoculated plants were then returned to growth chambers and maintained for the times indicated for each experiment. For longer experiments (lasting longer than ~30 days post-inoculation), plant growth

tubes were refilled with sterile-filered nanopure water as needed. To minimize cross-contamination, inoculated plants and non-inoculated plants were cultivated in separate growth chambers, and growth chambers were sterilized with 70% ethanol followed by UV irradiation for at least 24 hours between experiments.

Acetylene reduction experiments
Individual plants were transferred to clear glass 150 mL Balch-type anaerobic culture bottles containing 15 mL BNM medium and sealed under a gas-tight septum. After sealing, 15 mL of headspace gas (10% of the culture bottle volume) was removed and replaced with 15 mL of acetylene gas (Airgas). Plants in culture bottles were incubated in the light at 28°C in growth chambers for 3-6 hours. A 100 µl sample of the headspace gas was removed using a gas-tight syringe (Hamilton), and this sample was injected and analyzed for ethylene signal intensities using a Hewlett Packard 5890 Series II GC with Hewlett Packard 5972 Mass Spectrometer with a 30mx0.320mm GasPro Column (Agilent Technologies) and a 2 mm ID splitless liner (Restek Corporation). Following acetylene reduction measurements, plants were removed from jars and plant shoot heights and number of nodules per plant were recorded. When nodule dry mass measurements were performed, nodules were harvested with a razor blade, transferred into pre-weighed Eppendorf tubes, dried at 50°C for a minimum of 48 hours, then weighed again.

Live:Dead staining and imaging of nodule cross-sections
Nodules were hand-sectioned with razor blades and immediately transferred into a fresh solution of 5 µM SYTO9 (diluted 1:100 from a 500 uM stock in DMSO at -20°C; Thermo Fisher) and 0.02 mg/mL (30 µM) propidium iodide (diluted 1:50 from a 1 mg/mL stock stored in water at 4°C; Thermo Fisher) in PBS. Nodule sections were incubated in this SYTO9/propidium iodide solution at room temperature for 30 minutes in the dark with gentle shaking, washed 5X in PBS, and fixed in 4% paraformaldehyde (Electron Microscopy Sciences) in PBS overnight in the dark at 4°C. Fixed sections were washed 5X in PBS and transferred to a freshly prepared solution of 0.1 mg/mL Calcofluor White (Fluorescence Brightener 28; Sigma) in PBS. The sections were incubated in the Calcofluor solution in the dark for 1 hour at RT with gentle shaking and washed 5X in PBS to remove excess dye.

Prior to imaging, sections were transferred to 30 mm imaging dishes with 20 mm, #0 coverglass bottoms (MatTek) and overlaid with sterile 50% glycerol. Nodule images were collected on a Leica TCS SPE laser-scanning confocal (model DMI4000B-CS) using a 10X/0.3 NA APO ACS objective and solid-state laser lines for fluorophore excitation at the following settings for each dye: Calcofluor, 405 nm excitation/410-500 nm emission; SYTO9, 488 nm excitation/510-570 nm emission; PI, 532 nm excitation/600-650 nm emission. These images were then processed to enhance brightness and contrast in FIJI[57,58].

Nodule diameter and volume measurements
Inoculated *A. afraspera* root nodules were imaging using a high-definition Keyence VHX-600 digital microscope at 20X magnification. For end-point root nodule volume measurements at 40 days post-inoculation, plants were removed from the growth chamber and imaged at RT on paper towels, then discarded. Nodule diameters were measured using the line tool in FIJI and recorded using a custom FIJI macro. For tracking nodule volumes over time, plants were serially removed from their growth chambers and transferred to a plastic dish containing 150 mL of sterile BNM pre-warmed to 28°C. Images of sections of the plant root were collected serially from the hypocotyl to the root tip. Following collection of images, plants were immediately returned to their original growth tubes in the growth chamber. Plastic dishes were sterilized for 10 minutes in 10% bleach, washed three times in sterile-filtered nanopure water, sprayed with 70% ethanol/water, and air-dried before each new plant was imaged. A fresh aliquot of sterile, pre-warmed BNM also was used for each plant. After the time course was completed, images of entire plant root systems were reconstructed by eye for each plant at each time point. For nodules appearing in at least five time points, nodule diameters were measured as described for the end-point measurements and were converted to approximate volumes in R using the equation $V = 4/3\pi r^3$.

Nodule growth curve fitting and analysis
All analyses of nodule growth, and corresponding plots, were generated in R. For nodule growth curve fitting, three model equations were used to identify the best fit, as follows:

(1) exponential function:

$$V = ae^{-bt} + c$$

(2) quadratic function:

$$V = at^2 + bt + c$$

(3) generalized logistic function (expressed as a Richard's function with a time shift):

$$V = \frac{a}{(1 + e^{-b(t-c)})^{(\frac{1}{d})}}$$

Calculation of the optimal parameter values for each equation (e.g. the values of **a**, **b**, **c**, and **d**) and the standard error for each curve compared to the raw data were performed using the built-in function *nlm()* in R. In some cases, *nlm()* could not produce a best-fit model without specifying initial values for the function parameters. For exponential models, an equation of best fit could be successfully determined without specification of initial values for parameters **a**, **b** and **c**. For quadratic models, initial parameter values were required and were set to **a**=0, **b**=10 and **c**=0 for each nodule plot, after identifying these initial parameter values as broadly optimal based on an initial parameter sweep of -50 to 50 for each plot. For sigmoidal models, no broadly optimal initial values could be identified, so a parameter sweep was performed for each plot with the initial value of **a** set to the maximum observed nodule volume (as **a** describes the upper asymptote of the sigmoidal curve), **b** ranging from 0.1 to 1, **c** ranging from 0 to 10, and **d** ranging from 0.01 to 1.0. In the sigmoidal plots, an initial point of (0,0) was added to the nodule volume time series to improve fitting.

Because the sigmoidal model provided the best fits, extrapolation of nodule growth characteristics was performed on sigmoidal models only. The maximum nodule volume, V_{max}, is defined as the upper asymptote of the sigmoidal growth curve, *e.g.* **a**. The nodule initiation time, t_{min}, was defined in three separate ways: the times at which the nodule volume is equal to 0.05, 0.1, or 0.2 mm^3 (*e.g.* through solving 0.05, 0.1, or 0.2 = **a**/((1+e$^{(-b(t-c))}$)$^{(1/d)}$) for *t*). The maximum nodule growth rate, dV/dt, was defined as the average rate of growth (*e.g.* slope) between the time at which the volume is 10% of V_{max} and the time at which the volume is 90% of V_{max}. The time at which each nodule reaches its maximum size, t_{max}, was approximated as the time at which the volume is 90% of V_{max}, since the "true" maximum volume is asymptotic to the growth curve and is therefore never fully reached in the model.

Competition assays

mCherry-tagged Δ*hpnH* and YFP-tagged wild type *B. diazoefficiens* were grown to stationary phase (OD_{600} > 1.4) in 10 mL PSY cultures supplemented with 20 μg/mL (wild type) or 10 μg/mL (Δ*hpnH*) tetracycline; untagged strains were grown in PSY. On the day prior to inoculation, all strains were diluted into 50-150 mL tetracycline-free PSY to reach an OD_{600} of ~0.8 at the time of inoculation. *A. afraspera* plants were cultivated pre-inoculation in test tubes as described above, with the addition of covering the growth tubes in foil to minimize the production of chlorophyll in the plant roots, which spectrally overlaps with mCherry. At the time of inoculation, all cultures were pelleted at 3250 x g for 30 minutes at RT, washed three times, then resuspended in PSY to a final OD_{600} of 1.0. A 10 mL culture of each strain ratio for inoculation was generated a sterile 15mL Falcon tube; for example, for a 50:50 mixture of mCherry-tagged Δ*hpnH* and YFP-tagged wild type, 5 mL of each strain was combined. These cultures were mixed thoroughly by gentle pipetting, and 1 mL of the mixtures was added to directly to the plant medium for 7-8 plants per strain mixture.

After 45-60 days, plants were harvested. First, plant heights and the number of nodules per plant were recorded. Then, the roots were cut from the stem and images of all nodules for each plant were collected on a high-definition Keyence VHX-600 digital microscope at 20X magnification. These nodules were then cross-sectioned and immediately transferred to Eppendorfs containing 4% paraformaldehyde (Electron Microscopy Sciences) in PBS. Fresh sections were fixed overnight in the dark at 4°C, washed 5X in PBS, and stored in PBS supplemented with 0.1% azide in the dark at 4°C until imaging.

Fixed sections were stained in Calcofluor (all strain combinations), SYTO9 (WT-YFP and WT co-inoculation only) or propidium iodide (mCherry-Δ*hpnH* and Δ*hpnH* co-inoculation only) as described for Live:Dead staining. Imaging was performed as described for Live:Dead staining using a 5X objective.

Given the high autofluorescence of these nodules and low mCherry and YFP signal intensities, the following excitation/emission settings were used: Calcofluor, 405 nm excitation/410-460 nm emission; YFP/SYTO9, 488 nm excitation/500-550 nm emisasion; mCherry, 532 nm excitation/600-650 nm emission.

Quantification of nodule statistics (including nodule and infection zone areas, signal intensity of YFP, mCherry, SYTO9 and propidium iodide) was performed on raw images using a custom FIJI macro. Briefly, nodule images were opened at random, infection zones (IZs) and whole nodules were circled by hand and saved as discrete regions of interest (ROIs), and the area and intensity in each channel were measured automatically for all ROIs. These measurements were exported as a text table and various parameters from these measurements were calculated using custom Python scripts, as indicated in the Results. Plots of all parameters and statistical comparisons were generated using custom R scripts.

Antibiotic treatment of inoculated plants

A. afraspera plants were cultivated as described above and the following antibiotics were added to non-inoculated plants 7 days after rooting in 100 mL BNM growth tubes: kanamycin to 100 μg/mL, streptomycin to 100 μg/mL, tetracycline to 20 μg/mL, kanamycin plus tetracycline, kanamycin plus streptomycin, streptomycin plus tetracycline. Plants were grown in antibiotics under normal plant growth conditions for 14 days, after which plants were visually inspected. Plant heights were also recorded, and the root and shoot systems were separated with a razor blade, transferred into pre-weighed 15 mL Falcon tubes, dried at 50°C for a minimum of 48 hours, then weighed again.

Antibiotic treatments of ΔhpnH and wild-type *B. diazoefficiens* were performed by growing antibiotic 5 mL PSY cultures of each strain to stationary phase (OD_{600} >1.4) and diluting strains in fresh PSY to reach an OD_{600} of ~0.8 at the time of antibiotic treatment – *e.g.* as they would be grown prior to plant inoculation. Cultures were pelleted at 3250 x g for 30 minutes at RT, washed three times, then resuspended in PSY to a final OD_{600} of 1.0. Four 100 μl aliquots of these culture were diluted 1:00 into separate 10 mL BNM cultures in clear glass tubes in plant growth chambers. Kanamycin (at 25, 50, 75, and 100 μg/mL) and streptomycin (at 25, 50, 75, and 100 μg/mL) were added directly to the BNM cultures, and 100 μl samples were taken immediately prior to antibiotic treatment and at 2, 4, 6, 8, and 10 hours post-antibiotic addition. These 100 μl samples were immediately diluted 1:10 in 900 μl and mixed vigorously by repeated pipetting. Vortexing was avoided as we found that this method reduces ΔhpnH viability. Ten serial 1:10 dilutions were performed, and three 10 μl samples of each dilution for each strain were spotted and dripped across PSY plates. After 7 days (wild type) or 10 days (ΔhpnH), colonies were counted manually and recorded for each dilution exhibiting discrete colonies. Log plots of colony counts over time were generated in R.

Plants were then inoculated with ΔhpnH and wild-type *B. diazoefficiens* as described above, and kanamycin and streptomycin were added to ΔhpnH-inoculated plants to 50 μg/mL each, and to wild type-inoculated plants to 100 μg/mL at 12 hours and 36 hours and at 2, 2.5, 3, 3.5, 4, 4.5, 5, 6.5, 8.5, 9.5, 10.5, and 12.5 days post-inoculation. Four plants were treated per time point per strain, with an additional four plants each as an untreated control. At 40 dpi, the number of nodules per plant was recorded.

Bulk motility assays

Swimming motility assays were performed as previously described, with some modifications (Althabegoiti et al. 2008). WT and ΔhpnH were grown to turbidity in 5 mL of PSY at 30°C and 250 rpm, diluted to an OD_{600} of 0.02 in 5 mL of fresh PSY, and grown to exponential phase (OD_{600} = 0.3-0.5). Exponential cultures then were diluted to an OD_{600} of 0.06 in fresh PSY and 2 μL of the adjusted cultures into the center of swimming plate containing 0.3% agar/PSY. After inoculation, the plates were wrapped with parafilm to prevent dehydration and incubated in a humidity-controlled environmental chamber (Percival) at 30°C for 10 days total, with daily scans after 5 days. The resulting images were analyzed in FIJI to measure the area of the swimming colony.

Surface attachment assays

ΔhpnH and wild-type *B. diazoefficiens* were grown in 5 mL PSY cultures to stationary phase (OD_{600} >1.4) then diluted in fresh PSY to reach an OD_{600} of ~0.8 at the time of surface attachment assays. Cultures were pelleted at 3250 x g for 30 minutes at RT, washed twice in the indicated attachment medium, then resuspended in attachment medium to an OD_{600} of 1.0. These cultures were mixed thoroughly by repeated pipetting, and 2 mL samples were added to sterile imaging dishes (30 mm

dishes with 20 mm, #1.5 coverglass bottoms; MatTek). Cultures were incubated on imaging dishes *without shaking* at 30°C for two hours. To remove non-adhered cells, imaging dishes were immersed in 50 mL of attachment media in a 100 mL glass beaker on an orbital shaker and shaken gently at RT for 5 minutes; direct application of washing medium to the coverglass surface was avoided, as we found that this creates a shear force sufficient to wash away adhered cells. Imaging dishes were then gently lifted out of the washing medium and imaged with a 100X objective on a Lumascope 720 fluorescence microscope (Etaluma). Forty fields of view were recorded for each strain and media combination. These images were processed in FIJI using the Enhanced Local Contrast (CLAHE) plugin[59] and converted into a binary image to determine the area of the imaging window covered with adhered cells. Calculation of the fraction of the surface was performed in Excel and statistical analyses were conducted in R. Areas of the surface containing groups of cells larger than 10 μm^2 in area were ignored in the calculations, as these likely do not represent true attachment events rather than sedimentation of larger cell clumps. BNM used for attachment assays was prepared as described above, with the addition of 1.0 g/mL arabinose. Because BNM contains salt crystals that can sediment onto coverglass and occlude or obscure adhered cells, this medium was passed through a 2 μm filter (Millipore) prior to the attachment experiments.

Single-cell motility assays and analysis

B. diazoefficiens wild-type and ΔhpnH were grown in 12.5 ml PSY medium at 30°C and 200 rpm to an OD_{600} = 0.6-0.8 from an AG medium plate culture. Then, a 1:10 dilution of cell culture was subcultured in PSY medium to a final volume of 12.5 ml and regrown to an OD_{600} of ~0.6. Two aliquots of 750 µL were sampled from the regrowth culture and pelleted at 3500 x g for 20 min (wild-type) or for 30 min (ΔhpnH) at RT. The supernatant was removed, and one pellet was resuspended in 500 µL PSY and the other in 500 µL BNM medium. Because BNM contains salt crystals that can sediment onto coverglass and occlude or obscure adhered cells, this medium was passed through a 2 μm filter (Millipore) prior to usage for these experiments. The two medium conditions were then incubated for 2.5 hrs (wild-type) or for 3.5 hrs (ΔhpnH) at 30°C; given the difference in growth time ΔhpnH incubated for longer. Right before imaging, each culture was diluted at a 1:10 ratio with its respective medium. The bacteria were then injected into a sterile flow cell (ibidi sticky-Slide VI0.4 with a glass coverslip). The flow cell was attached to a heating stage set to 30°C.

The imaging protocol involved high-speed bright-field imaging for 5 min at a single XYZ location per experimental repeat. High speed bright-field recordings used a Phantom V12.1 high speed camera (Vision Research); images were taken with a 5 ms exposure at 200 fps and a resolution of 512×512 pixels (0.1 μm/pixel). This protocol was performed on an Olympus IX83 microscope equipped with a 100× oil objective, a 2× multiplier lens, and a Zero Drift Correction autofocus system. The recorded movies were extracted into single frames from the .cine files using PCC 2.8 (Phantom Software). Image processing and cell tracking algorithms are adapted from previous work[34] and written in MATLAB R2015a (Mathworks).

We identified cells swimming near the surface as cells with a trajectory radius of gyration greater than 2.5 μm and a mean-squared displacement (MSD) slope greater than 1.5. Setting a minimum radius of gyration selects for cells with a minimum net translation on the across the surface, while a minimum MSD slope threshold ensured the cells are moving super-diffusively (MSD slope $\cong$ 1, diffusive motion; MSD slope $\cong$ 2, super-diffusive motion). For each tracked cell, the mean-speed, $\mathbf{v}$, was calculated by averaging a moving window, $\mathbf{w}$, of the displacement over the cell's full trajectory, using the following equation:

$$< v > = \ Avg\left(\sum_{t=1}^{N-w} \frac{\sqrt{(x_{t+w} - x_t)^2 + (y_{t+w} - y_t)^2}}{w} * f * p \right)$$

where $\mathbf{N}$ is the total number of points in the trajectory, $\mathbf{f}$ is the acquisition frame rate, and $\mathbf{p}$ is the pixel resolution. Here we set a window size, w= 40 frames. All analysis and visualizations from these experiments where done using MATLAB R2015a (Mathworks).

Acknowledgements

References

1.   Belin, B. J. *et al.* Hopanoid lipids: from membranes to plant-bacteria interactions. *Nat. Rev. Microbiol.* **16,** 304–315 (2018).

2.   Saenz, J. P. *et al.* Hopanoids as functional analogues of cholesterol in bacterial membranes. *Proc. Natl. Acad. Sci. U. S. A.* **112,** 11971–11976 (2015).

3.   Wu, C.-H., Bialecka-Fornal, M. & Newman, D. K. Methylation at the C-2 position of hopanoids increases rigidity in native bacterial membranes. *Elife* **4,** (2015).

4.   Fantini, J. & Barrantes, F. J. How cholesterol interacts with membrane proteins: an exploration of cholesterol-binding sites including CRAC, CARC, and tilted domains. *Front. Physiol.* **4,** 31 (2013).

5.   Ochs, D. *et al.* Cloning, Expression, and Sequencing of Squalene-Hopene Cyclase,. **174,** 298–302 (1992).

6.   Syren, P.-O., Henche, S., Eichler, A., Nestl, B. M. & Hauer, B. Squalene-hopene cyclases-evolution, dynamics and catalytic scope. *Curr. Opin. Struct. Biol.* **41,** 73–82 (2016).

7.   Welander, P. V, Coleman, M. L., Sessions, A. L., Summons, R. E. & Newman, D. K. Identification of a methylase required for 2-methylhopanoid production and implications for the interpretation of sedimentary hopanes. *Proc. Natl. Acad. Sci. U. S. A.* **107,** 8537–8542 (2010).

8.   Welander, P. V, Doughty, D. M., Wu, C., Mehay, S. & Roger, E. Identification and characterization of Rhodopseudomonas palustris TIE-1 hopanoid biosynthesis mutants. **10,** 163–177 (2012).

9.   Schmerk, C. L. *et al.* Elucidation of the Burkholderia cenocepacia hopanoid biosynthesis pathway uncovers functions for conserved proteins in hopanoid-producing bacteria. *Environ. Microbiol.* **17,** 735–750 (2015).

10. Silipo, A. *et al.* Covalently linked hopanoid-lipid A improves outer-membrane resistance of a Bradyrhizobium symbiont of legumes. *Nat. Commun.* **5,** 5106 (2014).

11. Kulkarni, G. *et al.* Specific hopanoid classes differentially affect free-living and symbiotic states of Bradyrhizobium diazoefficiens. *MBio* **6,** e01251-15 (2015).

12. Komaniecka, I. *et al.* Occurrence of an unusual hopanoid-containing lipid A among lipopolysaccharides from Bradyrhizobium species. *J. Biol. Chem.* **289,** 35644–35655 (2014).

13. Ricci, J. N. *et al.* Diverse capacity for 2-methylhopanoid production correlates with a specific ecological niche. *ISME J.* **8,** 675–684 (2014).

14. Ourisson, G., Albrecht, P. & Rohmer, M. The Hopanoids: palaeochemistry and biochemistry of a group of natural products. *Pure Appl. Chem.* **51,** 709–729 (1979).

15. Racolta, S., Juhl, P. B., Sirim, D. & Pleiss, J. The triterpene cyclase protein family: a systematic analysis. *Proteins* **80,** 2009–2019 (2012).

16. Rodríguez-Navarro, D. N., Oliver, I. M., Contreras, M. A. & Ruiz-Sainz, J. E. Soybean interactions with soil microbes, agronomical and molecular aspects. doi:10.1051/agro/2010023

17. Vilcheze, C., Llopiz, P., Neunlist, S., Poralla, K. & Rohmer, M. Prokaryotic triterpenoids: New hopanoids from the nitrogen-fixing bacteria Azotobacter vinelandii, Beijerinckia indica and Beijerinckia mobilis. *Microbiology* **140,** 2749–2753 (1994).

18. Parsons, R., Silvester, W. B., Harris, S., Gruijters, W. T. & Bullivant, S. Frankia vesicles provide inducible and absolute oxygen protection for nitrogenase. *Plant Physiol.* **83,** 728–731 (1987).

19. Abeysekera, R. M., Newcomb, W., Silvester, W. B. & Torrey, J. G. A freeze-fracture electron microscopic study of *Frankia* in root nodules of *Alnus incana* grown at three oxygen tensions. *Can. J. Microbiol.* **36,** 97–108 (1990).

20. Wheatley, R. M. & Poole, P. S. Mechanisms of bacterial attachment to roots. *FEMS Microbiol.*

Rev. **42,** 448–461 (2018).

21. Kanbe, M., Yagasaki, J., Zehner, S., Göttfert, M. & Aizawa, S.-I. Characterization of two sets of subpolar flagella in Bradyrhizobium japonicum. *J. Bacteriol.* **189,** 1083–9 (2007).

22. Quelas, J. I. *et al.* Swimming performance of Bradyrhizobium diazoefficiens is an emergent property of its two flagellar systems OPEN. (2016). doi:10.1038/srep23841

23. Althabegoiti, M. J. *et al.* Analysis of the role of the two flagella of Bradyrhizobium japonicum in competition for nodulation of soybean. *FEMS Microbiol. Lett.* **319,** 133–139 (2011).

24. López-García, S. L. *et al.* In-Furrow Inoculation and Selection for Higher Motility Enhances the Efficacy of Nodulation. *Agron. J.* **101,** 357 (2009).

25. Bonaldi, K. *et al.* Nodulation of Aeschynomene afraspera and A. indica by photosynthetic Bradyrhizobium Sp. strain ORS285: the nod-dependent versus the nod-independent symbiotic interaction. *Mol. Plant. Microbe. Interact.* **24,** 1359–1371 (2011).

26. Patriarca, E. J., Tatè, R., Ferraioli, S. & Iaccarino, M. Organogenesis of Legume Root Nodules. *Int. Rev. Cytol.* **234,** 201–262 (2004).

27. Ledermann, R., Bartsch, I., Remus-Emsermann, M. N., Vorholt, J. A. & Fischer, H.-M. Stable Fluorescent and Enzymatic Tagging of Bradyrhizobium diazoefficiens to Analyze Host-Plant Infection and Colonization. *Mol. Plant. Microbe. Interact.* **28,** 959–967 (2015).

28. Pierre, O. *et al.* Peribacteroid space acidification: A marker of mature bacteroid functioning in Medicago truncatula nodules. *Plant, Cell Environ.* **36,** 2059–2070 (2013).

29. Denison, R. F. & Okano, Y. Leghaemoglobin oxygenation gradients in alfalfa and yellow sweetclover nodules. *J. Exp. Bot.* **54,** 1085–1091 (2003).

30. Kereszt, A., Mergaert, P., Montiel, J., Endre, G. & Kondorosi, E. Impact of Plant Peptides on Symbiotic Nodule Development and Functioning. *Front. Plant Sci.* **9,** 1026 (2018).

31. Glazebrook, J., Ichige, A. & Walker, G. C. A Rhizobium meliloti homolog of the Escherichia coli peptide-antibiotic transport protein SbmA is essential for bacteroid development. *Genes Dev.* **7,** 1485–97 (1993).

32. Szparaga, A. & Kocira, S. Generalized logistic functions in modelling emergence of Brassica napus L. *PLoS One* **13,** 1–14 (2018).

33. Richards, F. J. NA Flexible Growth Function for Empirical Useo Title. *J. Exp. Bot* **10,** 290–301 (1959).

34. Lee, C. K. *et al.* Multigenerational memory and adaptive adhesion in early bacterial biofilm communities. *Proc. Natl. Acad. Sci. U. S. A.* **115,** 4471–4476 (2018).

35. Gupta, R., Sharma, M. & Mittal, A. Effects of membrane tension on nanopropeller driven bacterial motion. *J Nanosci Nanotechnol* **6,** 3854–3862 (2006).

36. Petrova, O. E. & Sauer, K. Sticky situations: Key components that control bacterial surface attachment. *J. Bacteriol.* **194,** 2413–2425 (2012).

37. Persat, A. Bacterial mechanotransduction. *Curr. Opin. Microbiol.* **36,** 1–6 (2017).

38. Mä, J., Driessen, R., Galajda, P., Keymer, J. E. & Dekker, C. *Bacterial growth and motility in sub-micron constrictions.* (2009).

39. Tuson, H. H. *et al.* Measuring the stiffness of bacterial cells from growth rates in hydrogels of tunable elasticity. *Mol. Microbiol.* **84,** 874–891 (2012).

40. Busset, N. *et al.* The Very Long Chain Fatty Acid (C26:25OH) Linked to the Lipid A Is Important for the Fitness of the Photosynthetic Bradyrhizobium Strain ORS278 and the Establishment of a Successful Symbiosis with Aeschynomene Legumes. *Front. Microbiol.* **8,** 1821 (2017).

41. Bradley, A. S. *et al.* Hopanoid-free Methylobacterium extorquens DM4 overproduces carotenoids and has widespread growth impairment. *PLoS One* **12,** e0173323 (2017).

42. Neubauer, C. *et al.* Lipid remodeling in Rhodopseudomonas palustris TIE-1 upon loss of hopanoids and hopanoid methylation. *Geobiology* **13,** 443–453 (2015).

43. Keymer, A. Cross-kingdom lipid transfer in arbuscular mycorrhiza symbiosis and beyond. *Curr. Opin. Plant Biol.* **44,** 137–144 (2018).

44. Ferguson, B. J. *et al.* Legume nodulation: The host controls the party. *Plant. Cell Environ.* (2018). doi:10.1111/pce.13348

45. Tsikou, D. *et al.* Systemic control of legume susceptibility to rhizobial infection by a mobile microRNA. *Science (80-.).* **6907,** eaat6907 (2018).

46. Boiero, L. *et al.* Phytohormone production by three strains of Bradyrhizobium japonicum and possible physiological and technological implications. *Appl. Microbiol. Biotechnol.* **74,** 874–880

(2007).

47. Hammad, Y. *et al.* A possible role for phenyl acetic acid (PAA) on Alnus glutinosa nodulation by Frankia. *Plant Soil* **254,** 193–205 (2003).

48. Podlešáková, K. *et al.* Rhizobial Synthesized Cytokinins Contribute to But Are Not Essential for the Symbiotic Interaction Between Photosynthetic Bradyrhizobia and *Aeschynomene* Legumes. *Mol. Plant-Microbe Interact.* **26,** 1232–1238 (2013).

49. Ledermann, R., Bartsch, I., Muller, B., Wulser, J. & Fischer, H.-M. A Functional General Stress Response of Bradyrhizobium diazoefficiens Is Required for Early Stages of Host Plant Infection. *Mol. Plant. Microbe. Interact.* **31,** 537–547 (2018).

50. Burghardt, L. T. *et al.* Select and resequence reveals relative fitness of bacteria in symbiotic and free-living environments. *Proc. Natl. Acad. Sci. U. S. A.* **115,** 2425–2430 (2018).

51. Sugiyama, A. & Yazaki, K. Root Exudates of Legume Plants and Their Involvement in Interactions with Soil Microbes. doi:10.1007/978-3-642-23047-9_2

52. Pini, F. *et al.* Bacterial Biosensors for in Vivo Spatiotemporal Mapping of Root Secretion. *Plant Physiol.* **174,** 1289–1306 (2017).

53. FAO. *Regional Overview of Food Security and Nutrition in Africa 2017. The food security and nutrition–conflict nexus: building resilience for food security, nutrition and peace*. (2017).

54. Delgado-Baquerizo, M. *et al.* A global atlas of the dominant bacteria found in soil. *Science* **359,** 320–325 (2018).

55. Regensburger, B. & Hennecke, H. RNA polymerase from Rhizobium japonicum. *Arch. Microbiol.* **135,** 103–109 (1983).

56. Ehrhardt, D. W., Atkinson, E. M. & Long, S. R. Depolarization of alfalfa root hair membrane potential by Rhizobium meliloti Nod factors. *Science* **256,** 998–1000 (1992).

57. Schindelin, J. *et al.* Fiji: An open-source platform for biological-image analysis. *Nature Methods* **9,** 676–682 (2012).

58. Schneider, C. A., Rasband, W. S. & Eliceiri, K. W. *NIH Image to ImageJ: 25 years of Image Analysis HHS Public Access*. *Nat Methods* **9,** (2012).

59. Heckbert, P. S. & Karel. *Graphics gems IV*. *Graphics gems IV* (AP Professional, 1994).

Figure Legends

Figure 1. (**a**) Chemical structure of the extended hopanoid 2-Methyl Bacteriohopanetetrol (2Me-BHT), consisting of a central pentacyclic core synthesized by the *shc* gene product, a C2 methylation site added by the product of *hpnP* (grey shading, left), and a tetrol group added by the *hpnH* product (grey shading, right). (**b**) Average shoot heights and nodules per plant at 24 dpi for *A. afraspera* plants inoculated with wild-type, ΔhpnH or ΔhpnP *B. diazoefficiens.* (**c**) Average acetylene reduction per plant and per nodule at 24 dpi for *A. asfrapera* plants inoculated with wild-type, ΔhpnH or ΔhpnP. (**d**) Representative confocal images of cross-sections of wild type- and ΔhpnH-infected nodules at 24 dpi illustrating plant cell walls (Calcofluor, cyan), live bacteria (SYTO9, yellow) and membrane-compromised bacteria and plant nuclei (propidium iodide, magenta). (**e**) Average nodule dry mass and acetylene reduction per nodule dry mass at 24 dpi for plants inoculated with wild-type, ΔhpnH or ΔhpnP. Data shown in (**b**), (**c**) and (**e**) was collected from n = 8 plants, with error bars representing one standard deviation. Results of two-tailed t-tests between wild type and ΔhpnH or ΔhpnP are denoted as follows: n.s., $p>0.01$; *, $p<0.01$; **, $p<0.001$; ***, $p<0.0001$.

Figure 1-S1. Confocal images of cross-sections of wild type-infected *A. afraspera* nodules at 24 dpi illustrating plant cell walls (Calcofluor, cyan), live bacteria (SYTO9, yellow) and membrane-compromised bacteria and plant nuclei (propidium iodide, magenta). Nodules were collected from 3 plants.

Figure 1-S2. Confocal images of cross-sections of ΔhpnH-infected *A. afraspera* nodules at 24 dpi illustrating plant cell walls (Calcofluor, cyan), live bacteria (SYTO9, yellow) and dead bacteria and plant nuclei (propidium iodide, magenta). Nodules were collected from 3 plants. White boxes highlight small nodules. White arrow indicates a likely plant defense reaction.

Figure 2. (**a**) Average acetylene reduction per plant (n=4 plants per bar) and (**b**) average nodule dry mass per plant (n=8 plants per bar) for *A. asfrapera* inoculated with wild-type or Δ*hpnH* over time. Error bars representing one standard deviation. Results of two-tailed t-tests between wild type and Δ*hpnH* are denoted as follows: n.s., p>0.05; *, p<0.05; ***, p<0.0001. (**c-d**) *A. afraspera* inoculated with wild type or Δ*hpnH* at (**c**) 20 dpi (left) and at (**d**) 40 dpi (right). (**e-f**) Distributions of nodule diameters at 40 dpi for *A. afraspera* inoculated with (**e**) Δ*hpnH* (right; n=268 nodules pooled from 10 plants) or (**f**) wild type (left; n=227 nodules pooled from 10 plants).

Figure 2-S1. Average (**a**) shoot height, (**b**) nodules per plant, (**c**) nodule dry weight per plant, (**d**) acetylene reduction per plant, (**e**) acetylene reduction per nodule, and (**f**) acetylene reduction per nodule dry weight for *A. asfrapera* inoculated with wild-type or Δ*hpnH* at 40 dpi. N=4 plants per bar; error bars represent one standard deviation. Results of two-tailed t-tests between wild type and Δ*hpnH* are denoted as follows: n.s., p>0.05.

Figure 3. (**a**) Comparison of the development of selected wild type- and Δ*hpnH*-infected nodules over time. (**b**) Nodule growth plots for 74 wild type-infected nodules tracked from 10 plants. (**c**) Nodule growth plots for 84 Δ*hpnH*-infected nodules tracked from 16 plants. (**d**) Schematic of nodule development in *A. afraspera*. From the left, bacteria (in blue) colonize and invade plant roots (green) and intracellularly infect a root cell (pink); the time of this initial intracellular infection is considered t_i and the nodule volume can be described as the volume of the single infected root cell, V_i. This infected cell proliferates to form a spherical nodule that is visible to the naked eye, at time t_{min} and volume V_{min}. The infected plant cells continue to proliferate at rate dV/dt until the nodule has fully matured at time t_{max} and volume V_{max}. (**e**) Fitted growth curve for a sample wild-type nodule illustrating the positions of t_{min}, V_{min}, dV/dt, t_{max}, and V_{max}. (**f-g**) Jitter and box plots of (**f**) dV/dt and (**g**) V_{max} values for all wild type- and Δ*hpnH*-infected nodules. Results of KS-tests between wild-type and Δ*hpnH* nodules are denoted as follows: ***, p<10^{-6}. (**h**) Scatter plots of dV/dt vs. V_{max} values for wild-type and Δ*hpnH* nodules. Values of dV/dt and V_{max} below what is observed in the wild-type dataset are highlighted in green. (**i**) Distributions of t_{min} values (as observed by eye) for nodules from wild type- (white bars) or Δ*hpnH*- (grey bars) infected plants. N=457 wild-type nodules across 20 plants and 479 Δ*hpnH* nodules across 20 plants.

Figure 3-S1. Reconstructed images of the root system of a wild type-infected *A. afraspera* plant. Nodules fully visible in at least five time points are indicated with black arrowheads.

Figure 3-S2. Reconstructed images of the root system of a Δ*hpnH*-infected *A. afraspera* plant. Nodules fully visible in at least five time points are indicated with black arrowheads.

Figure 3-S3. Nodule growth plots for all 74 wild type-infected nodules fit with quadratic (orange; long dashed lines), exponential (yellow; short dashed lines), or sigmoidal (blue; solid lines) models. Standard errors (SE) for each model are shown.

Figure 3-S4. Nodule growth plots for all 84 Δ*hpnH*-infected nodules fit with quadratic (orange; long dashed lines), exponential (yellow; short dashed lines), or sigmoidal (blue; solid lines) models. Standard errors (SE) for each model are shown.

Figure 3-S5. (**a**) Jitter and box plots of t_{max} values for all wild type- and Δ*hpnH*-infected nodules. (**b**) Jitter and box plots of maximum growth windows for all wild type- and Δ*hpnH*-infected nodules. (**c**) Jitter and box plots of t_{min} values (as determined by extrapolation using sigmoidal fits of nodule growth curves) for all wild type- and Δ*hpnH*-infected nodules, in which V_{min} is defined as 0.05 mm^3, 0.1 mm^3, 0.2 mm^3. Green shading highlights negative t_{min} values. Results of KS-tests between wild-type and Δ*hpnH* nodules are denoted as follows: *, p<0.05; n.s., p>0.05.

Figure 3-S6. (**a-b**) Scatter plots of t_{max} vs. (**a**) dV/dt and (**b**) V_{max} for all wild type- (open circles) and Δ*hpnH*- (grey circles) infected nodules. Green regions highlight values below what is observed for wild type. (**c-d**) Scatter plots of maximum growth windows vs. (**c**) dV/dt and (**d**) V_{max}. (**e-f**) Scatter plots of t_{min} vs. (**c**) dV/dt and (**d**) V_{max}. (**g-h**) Scatter plots of t_{min} vs. (**a**) t_{max} and (**b**) maximum growth windows.

Figure 4. (**a**) Confocal sections of small (<0.5 mm radius) Δ*hpnH*-infected nodules harvested at 40 dpi and small (<0.5 mm radius) wild type-infected nodules harvested at 10 and 25 dpi. (**b**) Confocal sections of larger (>0.5 mm radius) Δ*hpnH*- or wild type-infected nodules harvested at 40 dpi.

Figure 4-S1. Confocal sections of small (<0.5 mm radius) Δ*hpnH*-infected nodules harvested at 40 dpi. Sections were stained with Calcofluor (cyan), SYTO9 (yellow), and propidium iodide (magenta). N=74 nodules harvested from 5 plants. White boxes highlight under-infected nodules. Magenta boxes indicate nodules primarily containing membrane-compromised cells.

Figure 4-S2. Confocal sections of large (>0.5 mm radius) Δ*hpnH*-infected nodules harvested at 40 dpi. Sections were stained with Calcofluor (cyan), SYTO9 (yellow), and propidium iodide (magenta). N=87 nodules harvested from 5 plants. White boxes highlight under-infected nodules.

Figure 4-S3. Confocal sections of small (<0.5 mm radius) wild type-infected nodules harvested at 10 dpi. Sections were stained with Calcofluor (cyan), SYTO9 (yellow), and propidium iodide (magenta). N=80 nodules harvested from 5 plants. White boxes highlight under-infected nodules.

Figure 4-S4. Confocal sections of small (<0.5 mm radius) wild type-infected nodules harvested at 25 dpi. Sections were stained with Calcofluor (cyan), SYTO9 (yellow), and propidium iodide (magenta). N=82 nodules harvested from 5 plants. Magenta boxes indicate nodules primarily containing membrane-compromised cells.

Figure 4-S5. Confocal sections of wild type-infected nodules harvested at 40 dpi. Sections were stained with Calcofluor (cyan), SYTO9 (yellow), and propidium iodide (magenta). N=117 nodules harvested from 5 plants. Magenta boxes indicate nodules primarily containing membrane-compromised cells.

Figure 5. (**a**) Confocal sections of nodules from plants co-inoculated with wild type-YFP and Δ*hpnH*-mCherry harvested at 45-55 dpi. Sections were stained with Calcofluor (cyan) and are expressing YFP (yellow) and mCherry (magenta). (**b**) Scatter plot of median YFP intensity per pixel normalized by propidium iodide intensity per pixel (*e.g.* bacteroid density) within infection zones of nodules from plants co-inoculated with wild type-YFP and wild type, as a function of the percentage of wild type-YFP in the inoculum. (**c**) Scatter plot of median propidium iodide intensity per pixel (*e.g.* bacteroid density) within infection zones of nodules from plants co-inoculated with YFP-tagged wild type and untagged wild type, as a function of the percentage of WT-YFP in the inoculum. (**d**) Colony forming units/mL in wild type and Δ*hpnH* cultures grown in BNM supplemented with varying concentrations of kanamycin and spectinomycin at various times post-inoculation. (**e**) Average nodules per plant at 40 dpi for plants inoculated with either wild type or Δ*hpnH* and treated with 50 μg/mL (Δ*hpnH*) or 100 μg/mL (wild type) kanamycin and streptomycin at various time points post-inoculation. Nodule counts are normalized to those observed in non-antibiotic treated plants. (**f**) Images of inoculated plants at 40 dpi after antibiotic treatment at various time points. Untreated plants are shown on the left, with increasing time of antibiotic addition. Error bars represent one standard deviation.

Figure 5-S1. Confocal sections of nodules from plants co-inoculated with 10% WT-YFP:90% Δ*hpnH*-mCherry. Nodules were harvested between 45 and 50 dpi. Sections were stained with Calcofluor (cyan) and express YFP (yellow) mCherry (magenta). N=132 nodules harvested from 8 plants.

Figure 5-S2. Confocal sections of nodules from plants co-inoculated with 25% WT-YFP:75% Δ*hpnH*-mCherry. Nodules were harvested between 45 and 50 dpi. Sections were stained with Calcofluor (cyan) and express YFP (yellow) mCherry (magenta). N=125 nodules harvested from 7 plants.

Figure 5-S3. Confocal sections of nodules from plants co-inoculated with 50% WT-YFP:50% Δ*hpnH*-mCherry. Nodules were harvested between 45 and 50 dpi. Sections were stained with

Calcofluor (cyan) and express YFP (yellow) mCherry (magenta). N=143 nodules harvested from 7 plants.

Figure 5-S4. Confocal sections of nodules from plants co-inoculated with 75% WT-YFP:25% Δ*hpnH*-mCherry. Nodules were harvested between 45 and 50 dpi. Sections were stained with Calcofluor (cyan) and express YFP (yellow) mCherry (magenta). N=143 nodules harvested from 8 plants.

Figure 5-S5. Confocal sections of nodules from plants co-inoculated with 90% WT-YFP:10% Δ*hpnH*-mCherry. Nodules were harvested between 45 and 50 dpi. Sections were stained with Calcofluor (cyan) and express YFP (yellow) mCherry (magenta). N=110 nodules harvested from 7 plants.

Figure 5-S6. Average shoot height (**a**) and number of nodules (**b**) for plants co-inoculated with Δ*hpnH*-mCherry and WT-YFP strains, recorded at 45 dpi. Average shoot height (**c**) and number of nodules (**d**) for plants co-inoculated with WT and WT-YFP strains, recorded at 40 dpi. Average shoot height (**e**) and number of nodules (**f**) for plants co-inoculated with Δ*hpnH* and Δ*hpnH*-mCherry strains, recorded at 50 dpi. N=7-8 plants per bar for all panels. Error bars represent one standard deviation. Results of two-tailed t-tests are denoted as follows: n.s., p>0.05; ***, p<0.0001.

Figure 5-S7. (**a-d**) Intensity ratio of YFP to mCherry (**a**), mCherry intensity (**b**), and YFP intensity (**c**) per pixel within infection zones of nodules co-inoculated with Δ*hpnH*-mCherry and WT-YFP strains. (**d**) Cross-sectional area of infection zones of nodules co-inoculated with Δ*hpnH*-mCherry and WT-YFP strains. For (**a-d**), N=132, 125, 143, 143 and 110 nodules for 10%, 25%, 50%, 75% and 90% WT-YFP strain mixtures, respectively, which were sectioned and fixed between 45-50 dpi. (**e**) Nodule volume distributions from plants co-inoculated with Δ*hpnH*-mCherry and WT-YFP strains at 45 dpi. Sample sizes are N = 251, 200, 227, 204, and 149 nodules pooled from N = 8, 7, 7, 8, and 7 plants for the 10%, 25%, 50%, 75% and 90% WT-YFP strain mixtures, respectively. (**f**) Scatter plots of mCherry vs. YFP intensities per pixel within infection zones of nodules co-inoculated with Δ*hpnH*-mCherry and WT-YFP strains. (**g-h**) Scatter plots of YFP/mCherry intensity ratios per pixel in infection zones vs. infection zone (**g**) and nodule (**h**) cross-section areas for nodules co-inoculated with Δ*hpnH*-mCherry and WT-YFP strains. Scatter plots contain data pooled from all ratios.

Figure 5-S8. (**a-d**) Intensity ratio of YFP to propidium iodide (PI) (**a**), PI intensity (**b**), and YFP intensity (**c**) per pixel within infection zones of nodules co-inoculated with WT and WT-YFP strains. (**d**) Cross-sectional area of infection zones of nodules co-inoculated with WT and WT-YFP strains. For (**a-d**), N = 141, 95, 134, 147, 133, and 167 nodules for 10%, 25%, 50%, 75%, 90% and 100% WT-YFP strain mixtures, respectively, which were sectioned and fixed between 40-45 dpi. (**e**) Nodule volume distributions from plants co-inoculated with WT and WT-YFP strains at 40 dpi. Sample sizes are N = 183, 116, 161, 172, 232, and 248 nodules pooled from N = 8, 7, 8, 8, 8, and 8 plants for the 10%, 25%, 50%, 75% and 90% WT-YFP strain mixtures, respectively. (**f**) Scatter plots of PI vs. YFP intensities per pixel within infection zones of nodules co-inoculated with WT and WT-YFP strains. (**g-h**) Scatter plots of YFP/PI intensity ratios per pixel in infection zones vs. infection zone (**g**) and nodule (**h**) cross-section areas for nodules co-inoculated with WT and WT-YFP strains. Scatter plots contain data pooled from all ratios.

Figure 5-S9. (**a-d**) Intensity ratio of mCherry to SYTO9 (**a**), SYTO9 intensity (**b**), and mCherry intensity (**c**) per pixel within infection zones of nodules co-inoculated with Δ*hpnH*-mCherry and Δ*hpnH* strains. (**d**) Cross-sectional area of infection zones of nodules co-inoculated with Δ*hpnH*-mCherry and Δ*hpnH* strains. For (**a-d**), N = 117, 107, 128, 137, 103 and 50 nodules for 10%, 25%, 50%, 75%, 90% and 100% Δ*hpnH*-mCherry strain mixtures, respectively, which were sectioned and fixed between 50-55 dpi. (**e**) Nodule volume distributions from plants co-inoculated with Δ*hpnH*-mCherry and Δ*hpnH* strains at 45 dpi. Sample sizes are N = 150, 222, 191, 254, 297, and 236 nodules pooled from N = 7, 7, 7, 8, 8, and 8 plants for the 10%, 25%, 50%, 75% and

90% WT-YFP strain mixtures, respectively. (**f**) Scatter plots of mCherry vs. SYTO9 intensities per pixel within infection zones of nodules co-inoculated with Δ*hpnH*-mCherry and Δ*hpnH* strains. (**g-h**) Scatter plots of mCherry/SYTO9 intensity ratios per pixel in infection zones vs. infection zone (**g**) and nodule (**h**) cross-section areas for nodules co-inoculated with Δ*hpnH*-mCherry and Δ*hpnH* strains. Scatter plots contain data pooled from all strain ratios.

Figure 5-S10. Average (**a**) shoot height, (**b**) shoot dry mass and (**c**) root dry mass for non-inoculated *A. afraspera* plants grown in BNM supplemented with kanamycin, streptomycin or tetracycline for 2 weeks under normal growth conditions. N=4 plants per condition; error bars represent one standard deviation. (**d-e**) Images of *A. afraspera* plants after 2 weeks of antibiotic treatment. Asterisks indicate plants grown in tetracycline-supplemented medium.

Figure 6. (**a**) Sample time course of wild type and Δ*hpnH* colony expansion on low-agar PSY plates (dpi = days post-inoculation). Scale bars represent 2 cm. (**b**) Average colony sizes of wild type and Δ*hpnH* over time. N=4 plates per strain; error bars indicate one standard deviation. (**c**) Trajectories of individual wild type (top) and Δ*hpnH* (bottom) cells over a 5 minute time course in PSY. (**d**) Distributions of mean-speed s for motile wild type (N=359) and Δ*hpnH* (N=91) cells for trajectories in **d**. Dotted lines indicate the means of the distributions. (**e**) Trajectories of individual wild type (top) and Δ*hpnH* (bottom) cells over a 5 minute time course in BNM. (**f**) Distributions of mean-speeds for motile WT (N=421) and Δ*hpnH* (N=141) cells in BNM for trajectories in **e**. Dotted lines indicate the means of the distributions. (g) Jitter and box plots of surface attachment (*e.g.* the percent of the field of view covered with cells) of WT and Δ*hpnH* after 2 hours of incubation on glass in PSY or BNM. N=40 fields of view per condition. Results of two-tailed t-tests between wild type and Δ*hpnH* are denoted as follows: n.s., p>0.05; ***, p<0.00001.

Figure 6-S1. Surface attachment of wild type (**a,c**) and Δ*hpnH* (**b,d**) incubated on glass coverslips in various media. For each panel, raw phase images (top row), background-subtracted images (middle row), and binary images with cells shown in black (bottom row) are shown. Scale bars represent 20 µm.

Figure 7. Schematic representation of *A. afraspera* wild-type root nodule development (top row; white background) and defects in development associated with extended hopanoid loss (bottom row; grey background). Early in development, fewer Δ*hpnH* cells are motile (**a**) and competent to attach to root surfaces (**b**), leading to a delay in establishment of stable root colonies. At later stages, slow growth of Δ*hpnH* into the root interior, or poor uptake by and division within host cells (**c**) may generate "patchy", or under-populated infection zone that is propagated as the nodule grows (**d**). Alternately, fully-infected Δ*hpnH* nodules may lose symbionts to symbiont cell death (**e**) via poor bacteroid survival or plant-directed symbiosome degradation.
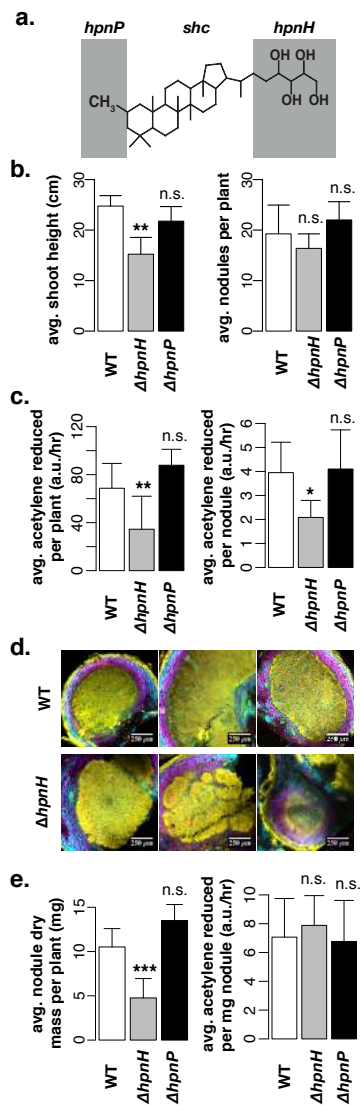
Figure 1.
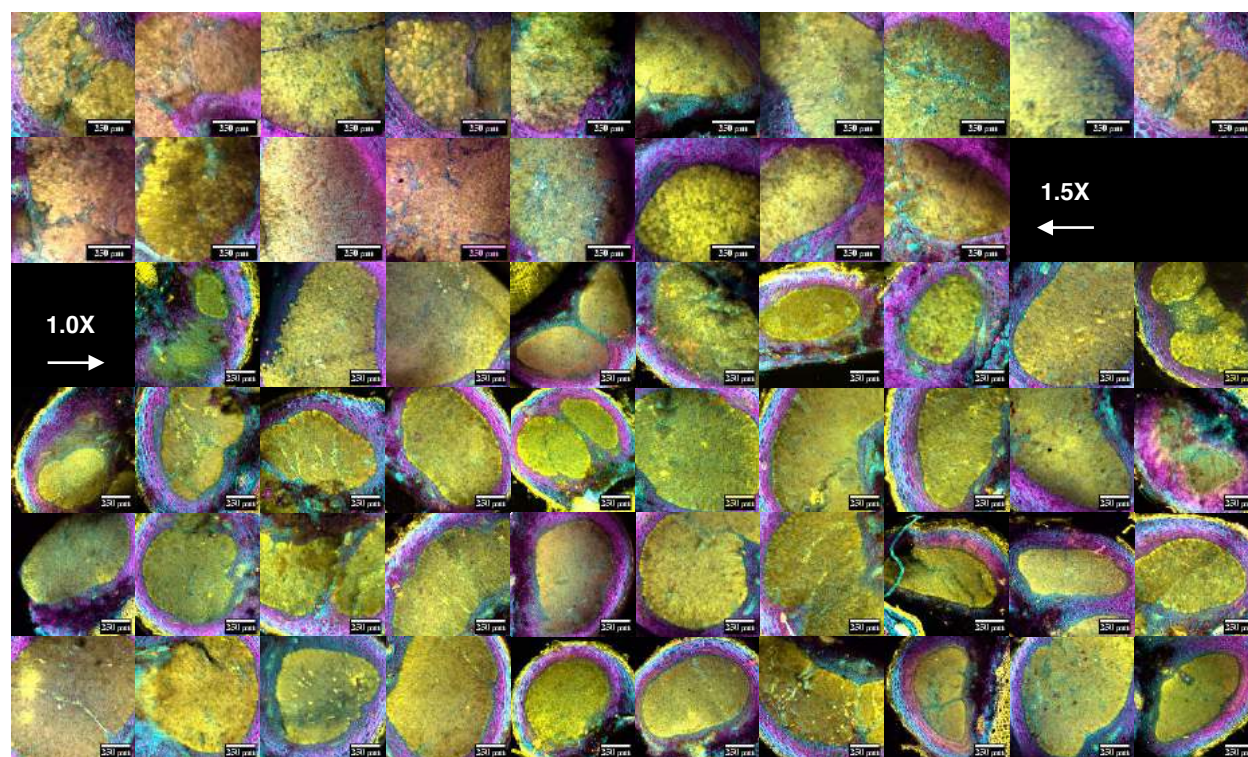
Figure 1-S1.
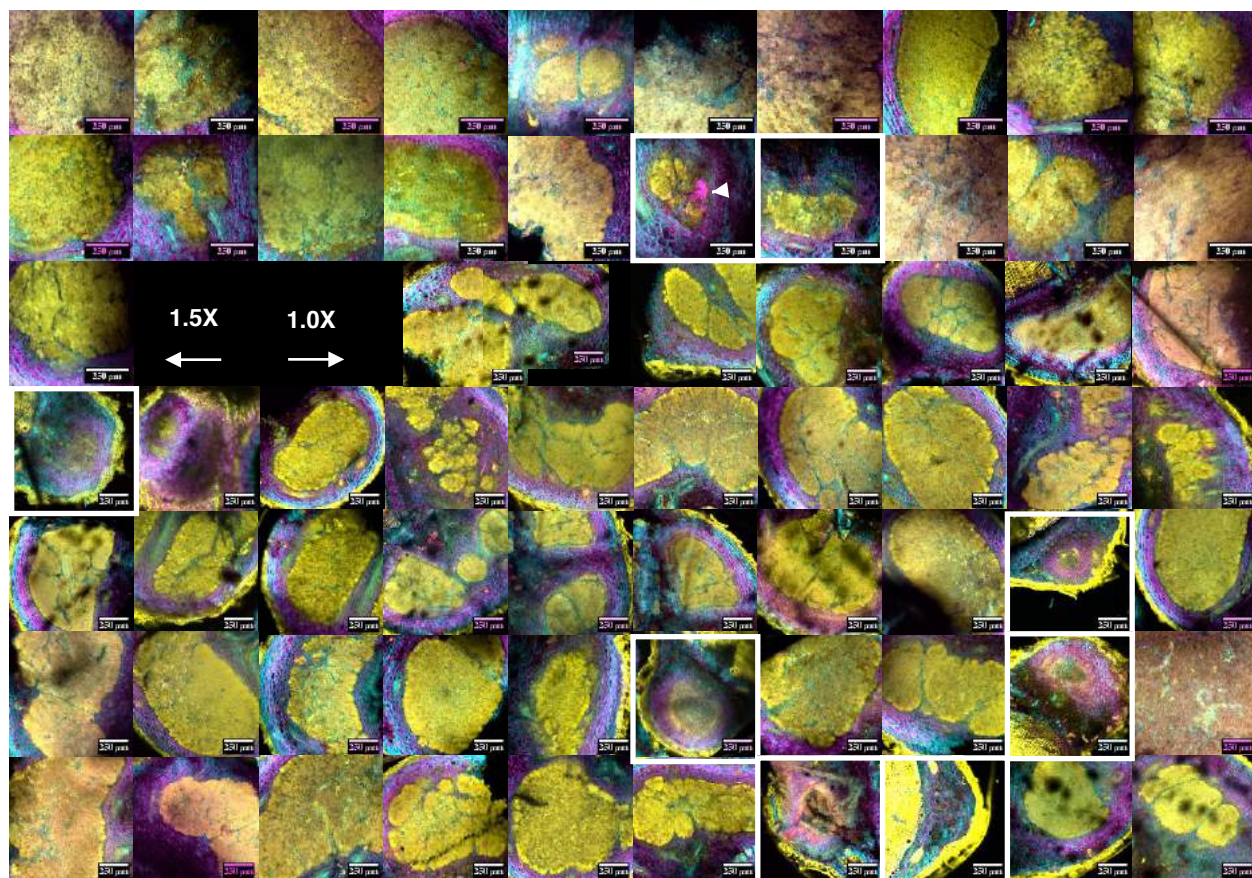
Figure 1-S2.
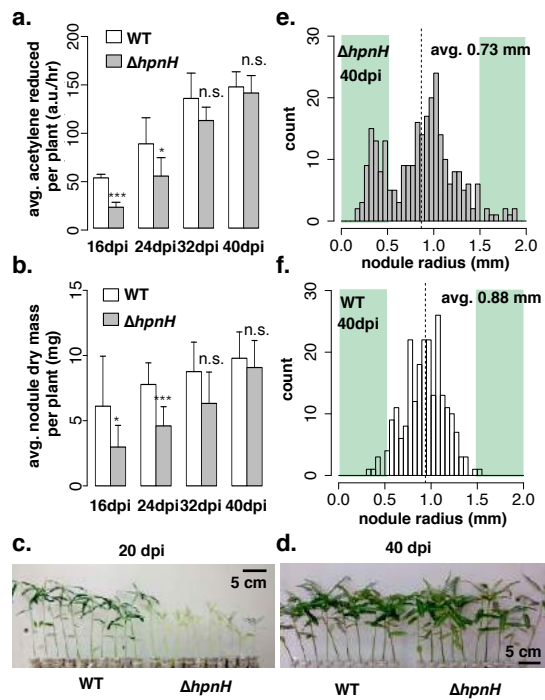
Figure 2.
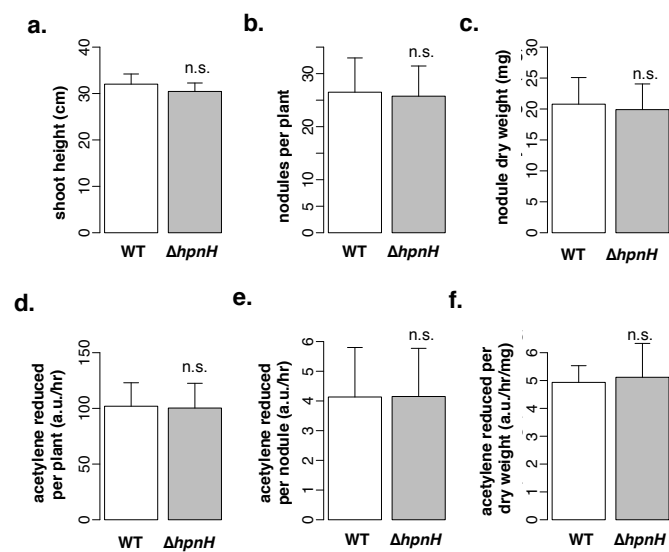
Figure 2-S1.
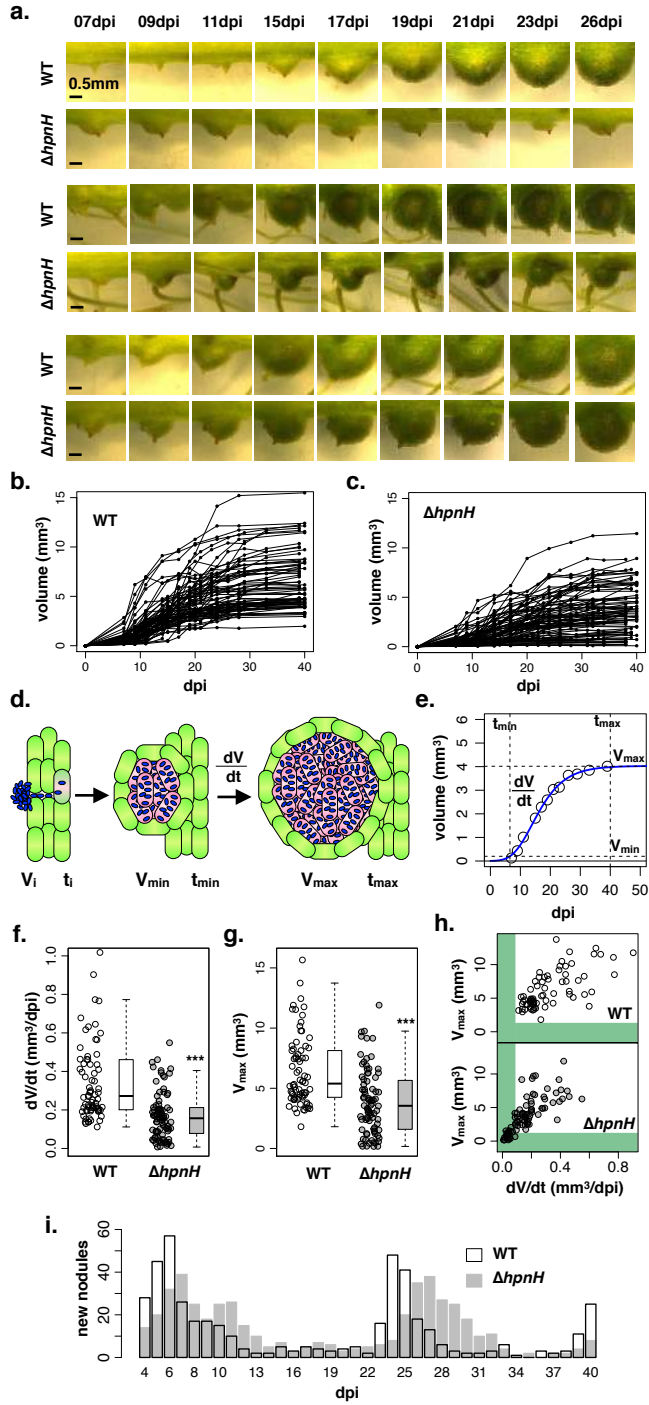
Figure 3.
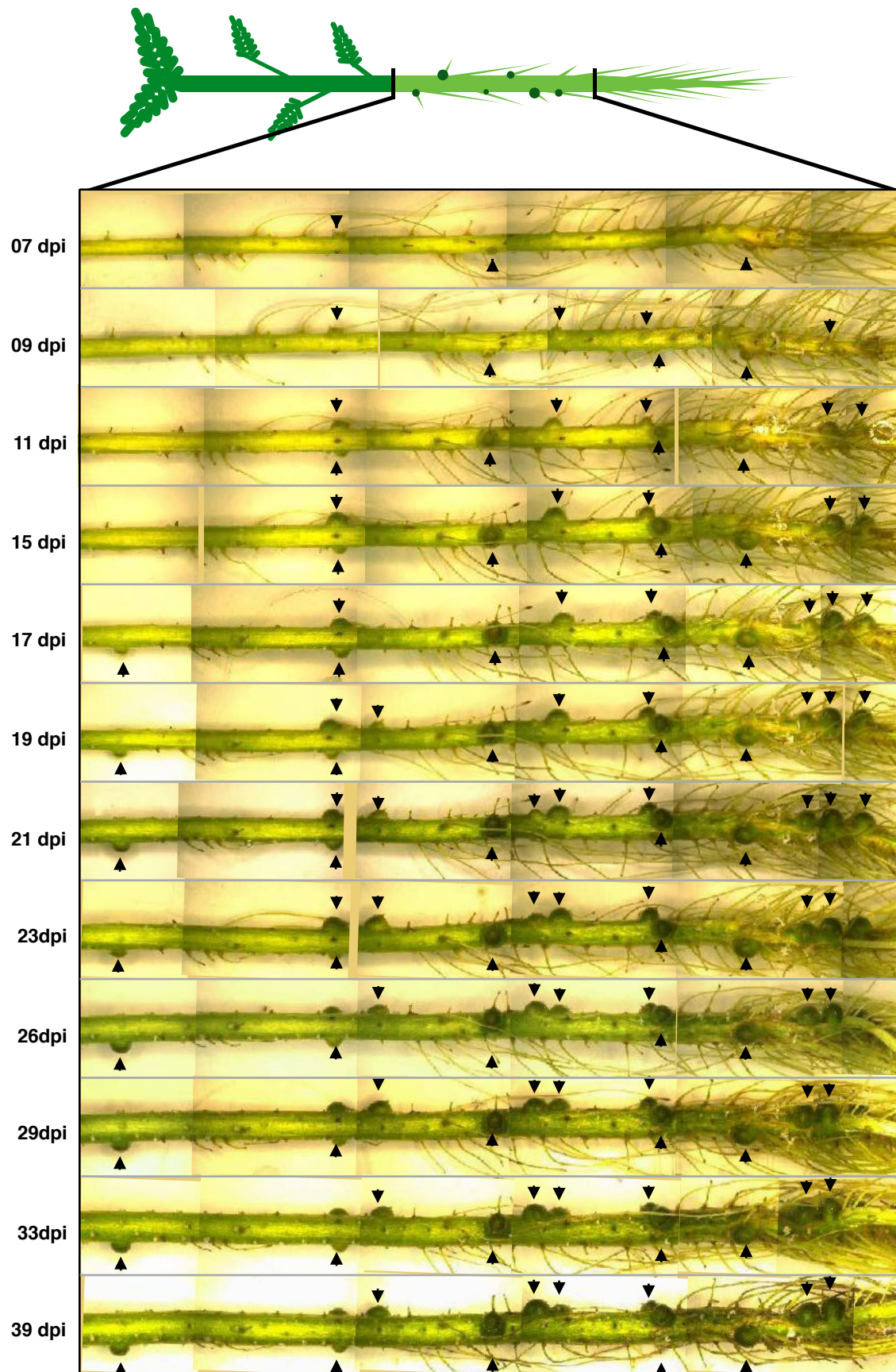
Figure 3-S1.
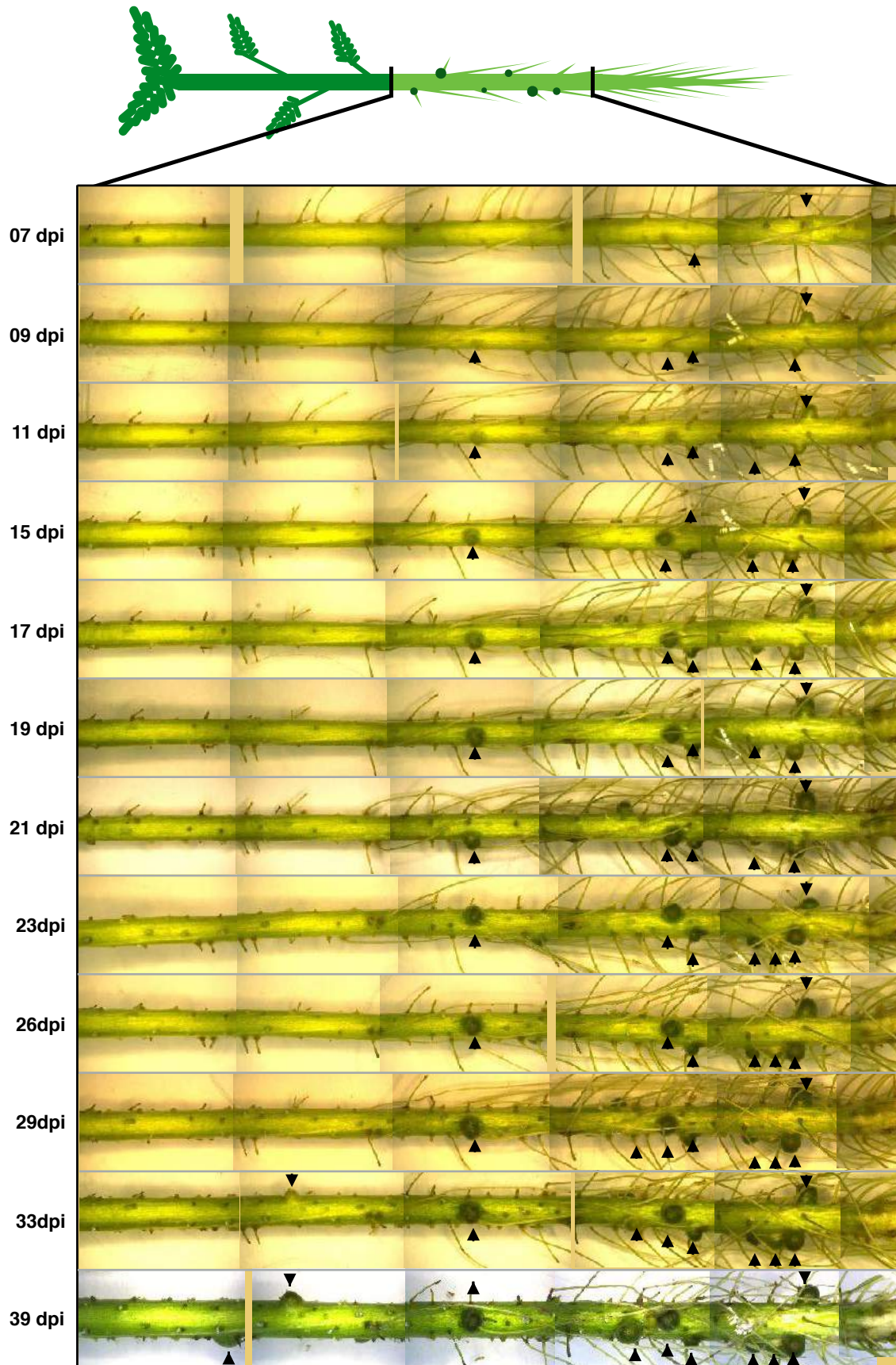
Figure 3-S2.
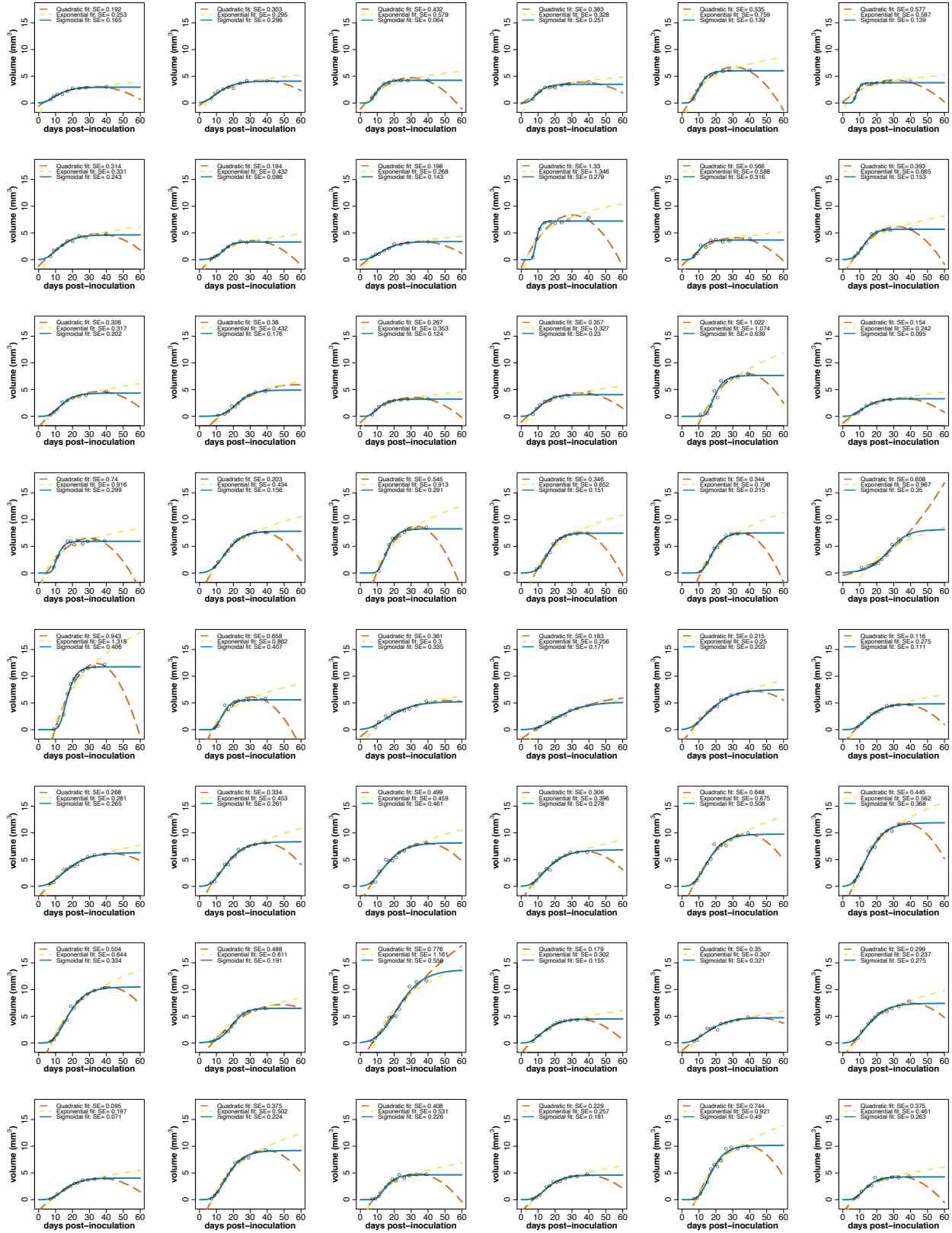
Figure 3-S3.
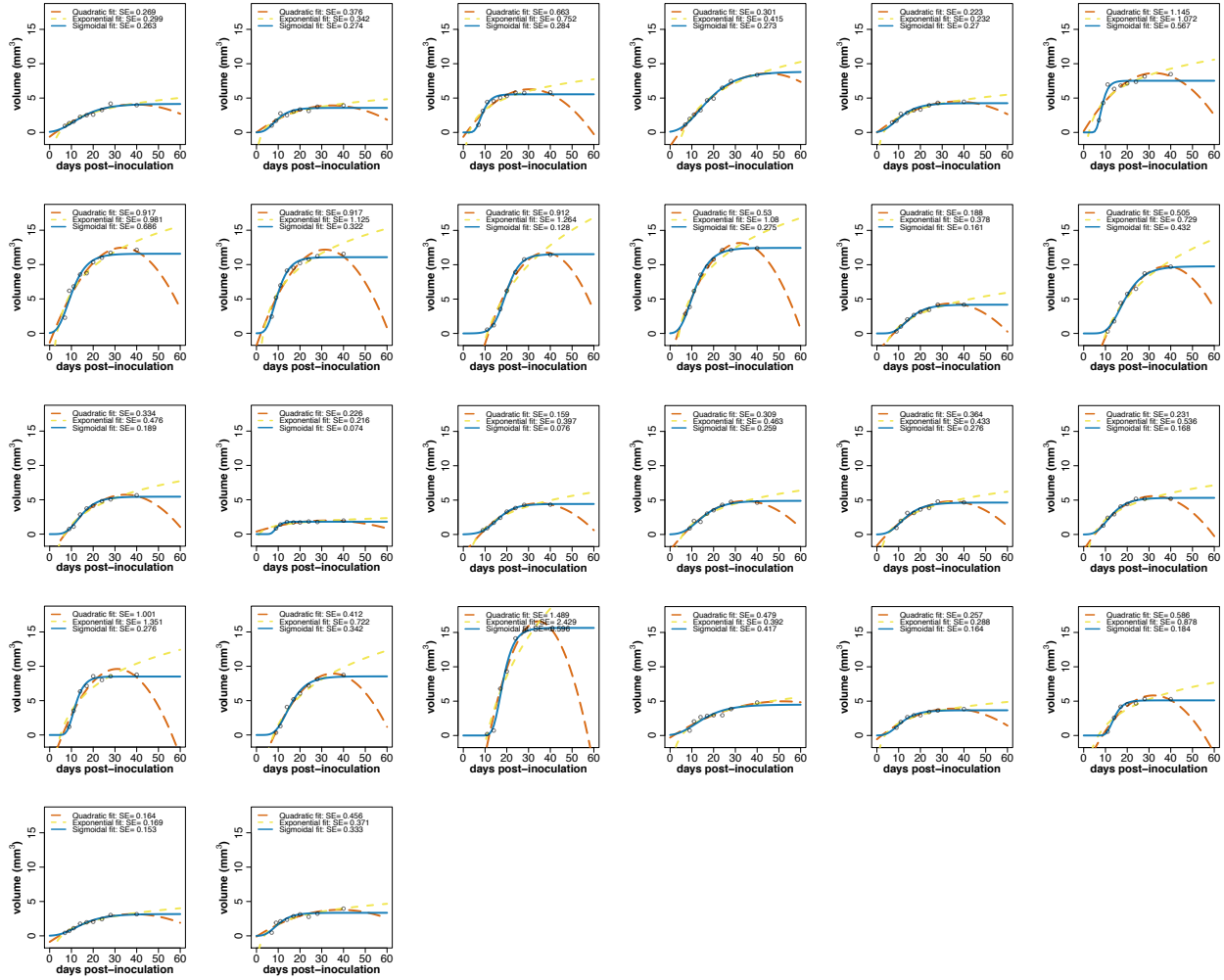
Figure 3-S3 cont.
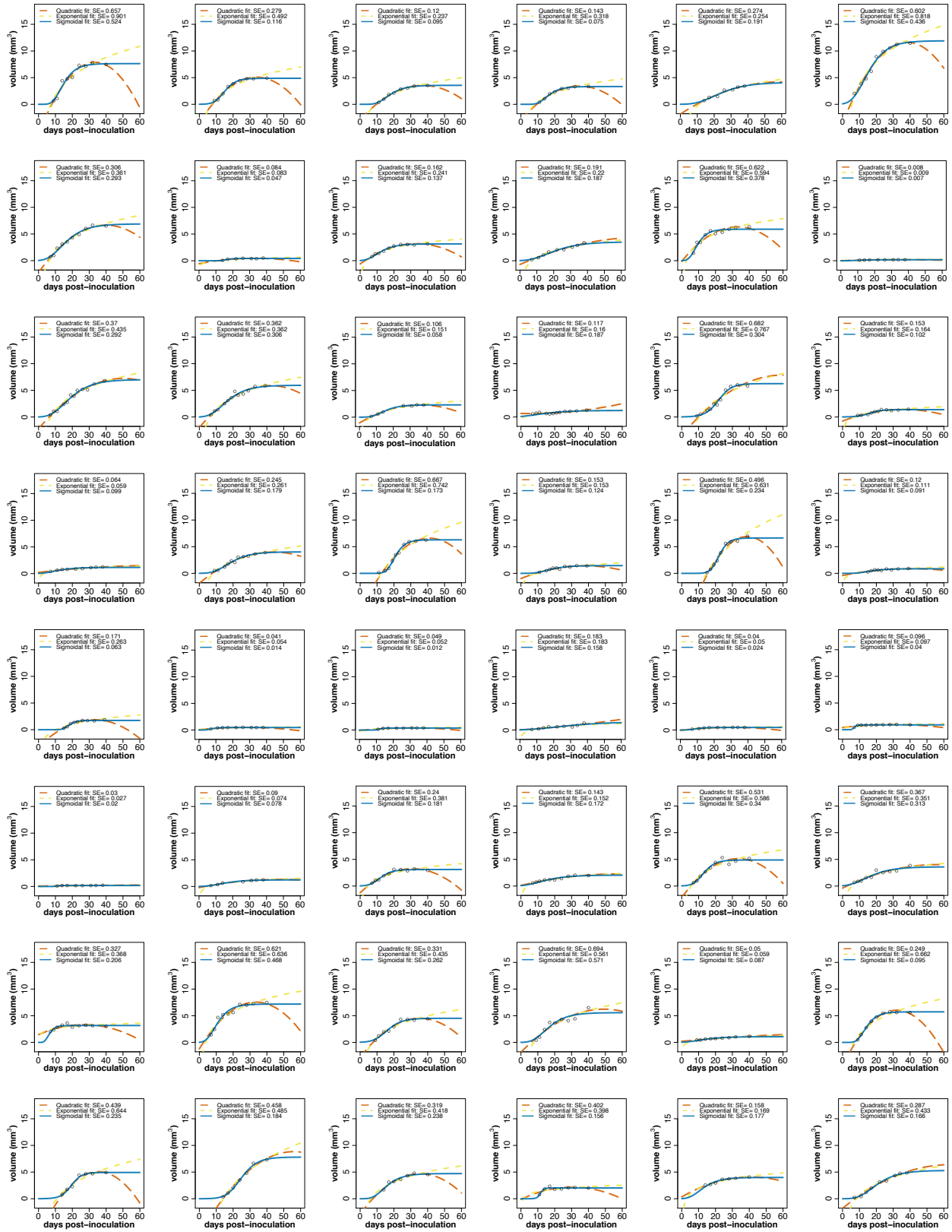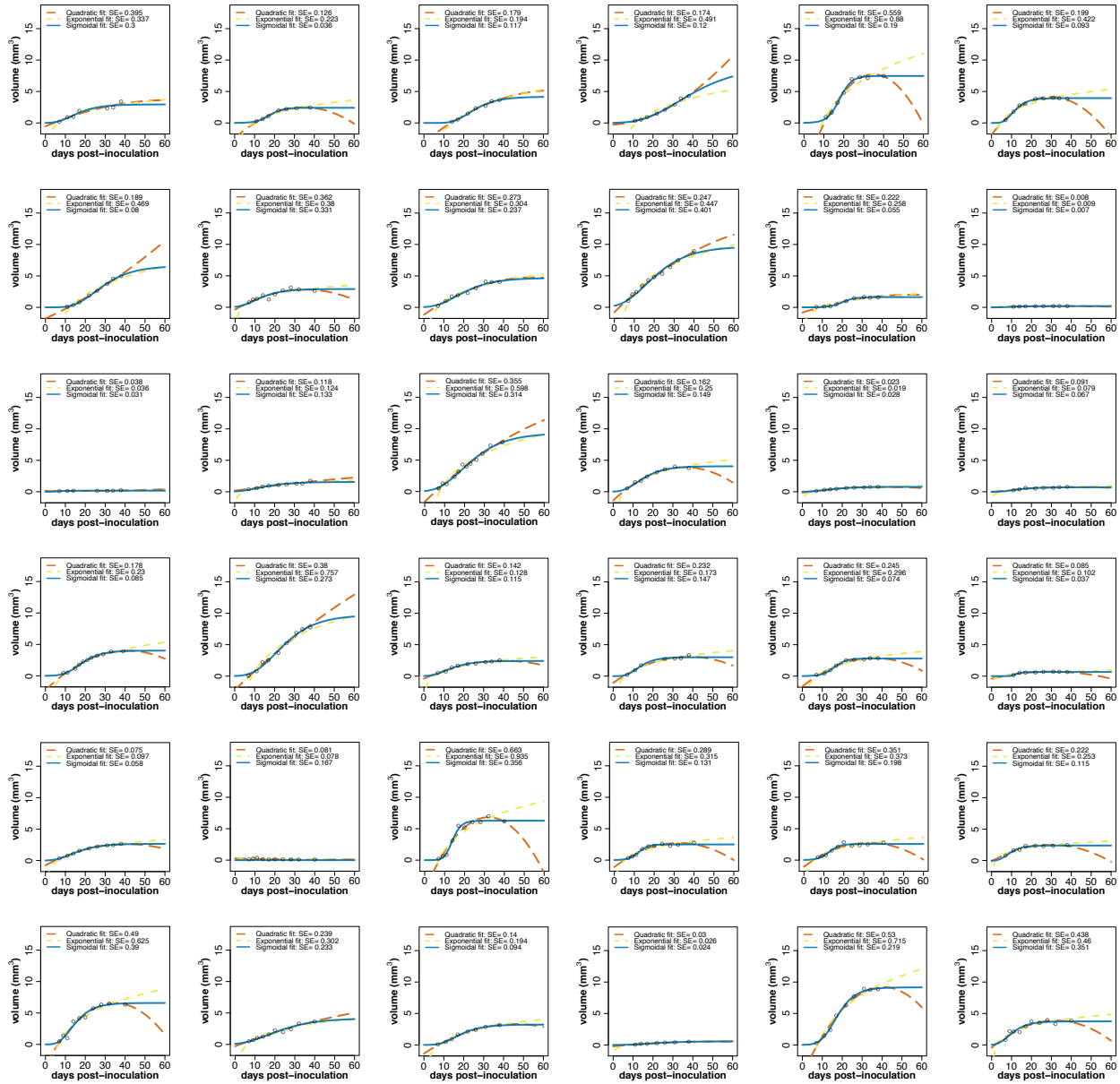
Figure 3-S4.

Figure 3-S4 cont.
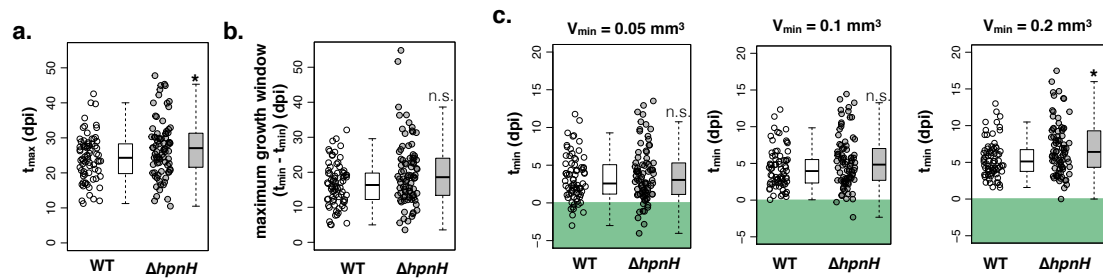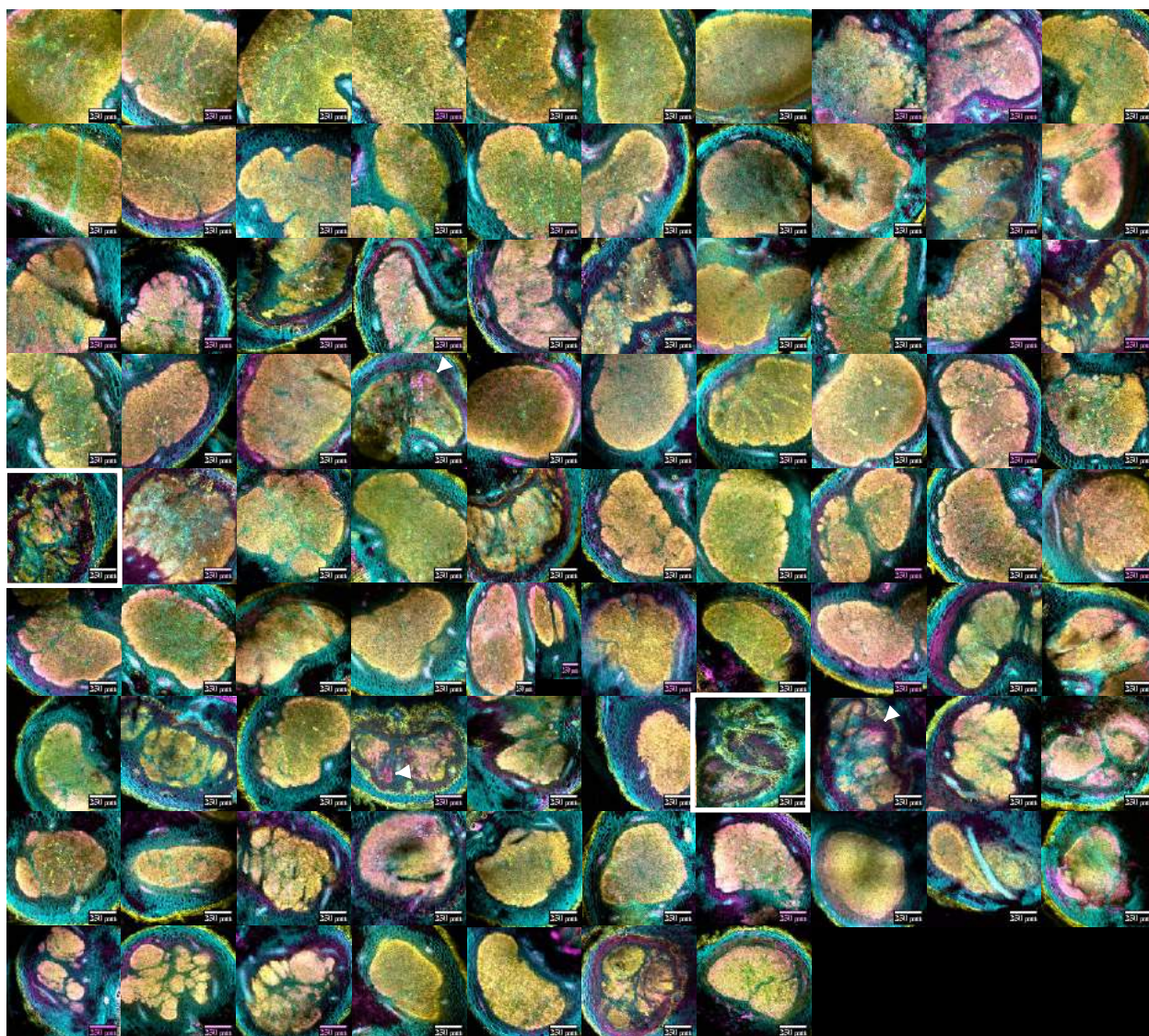
Figure 3-S5.
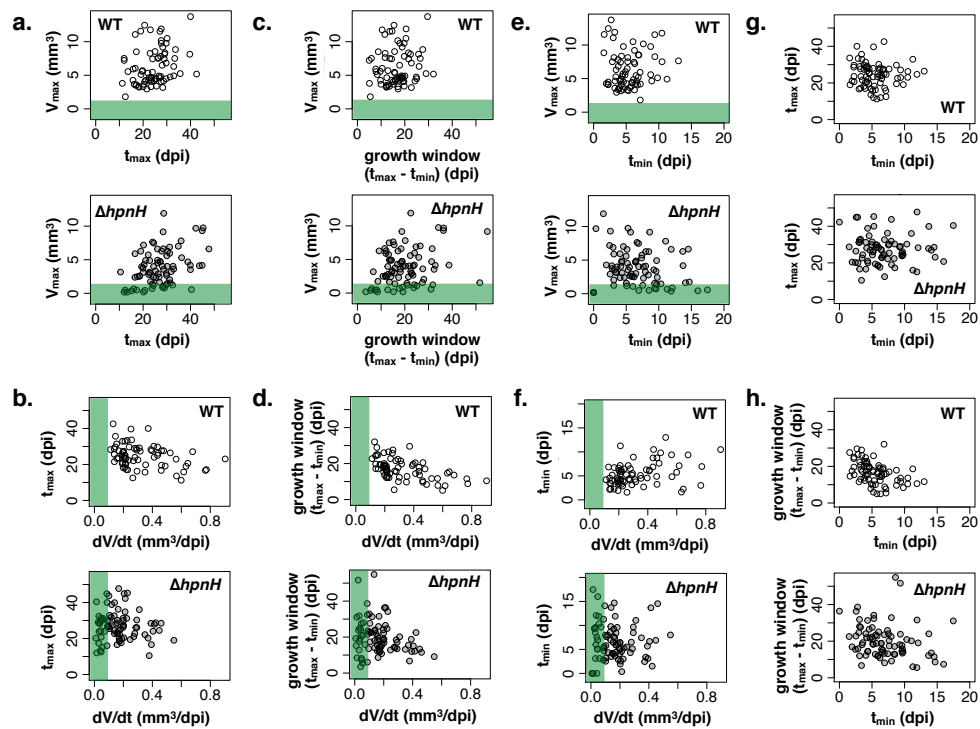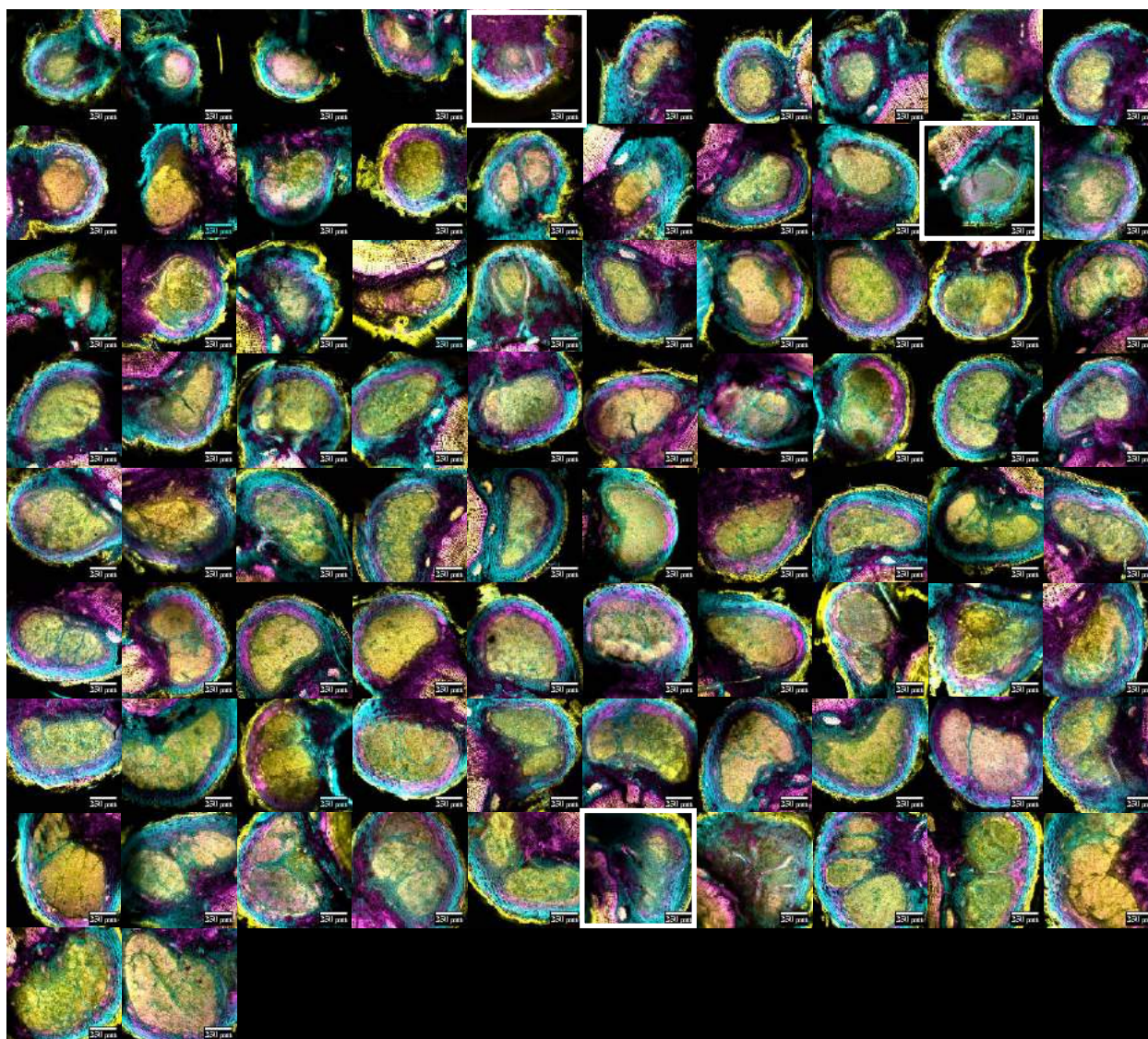
Figure 3-S6.
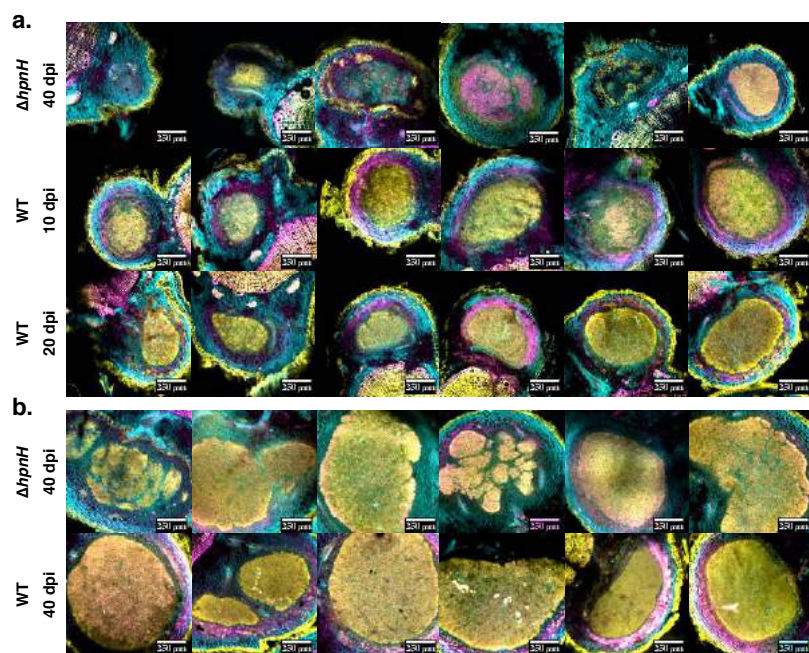
Figure 4.
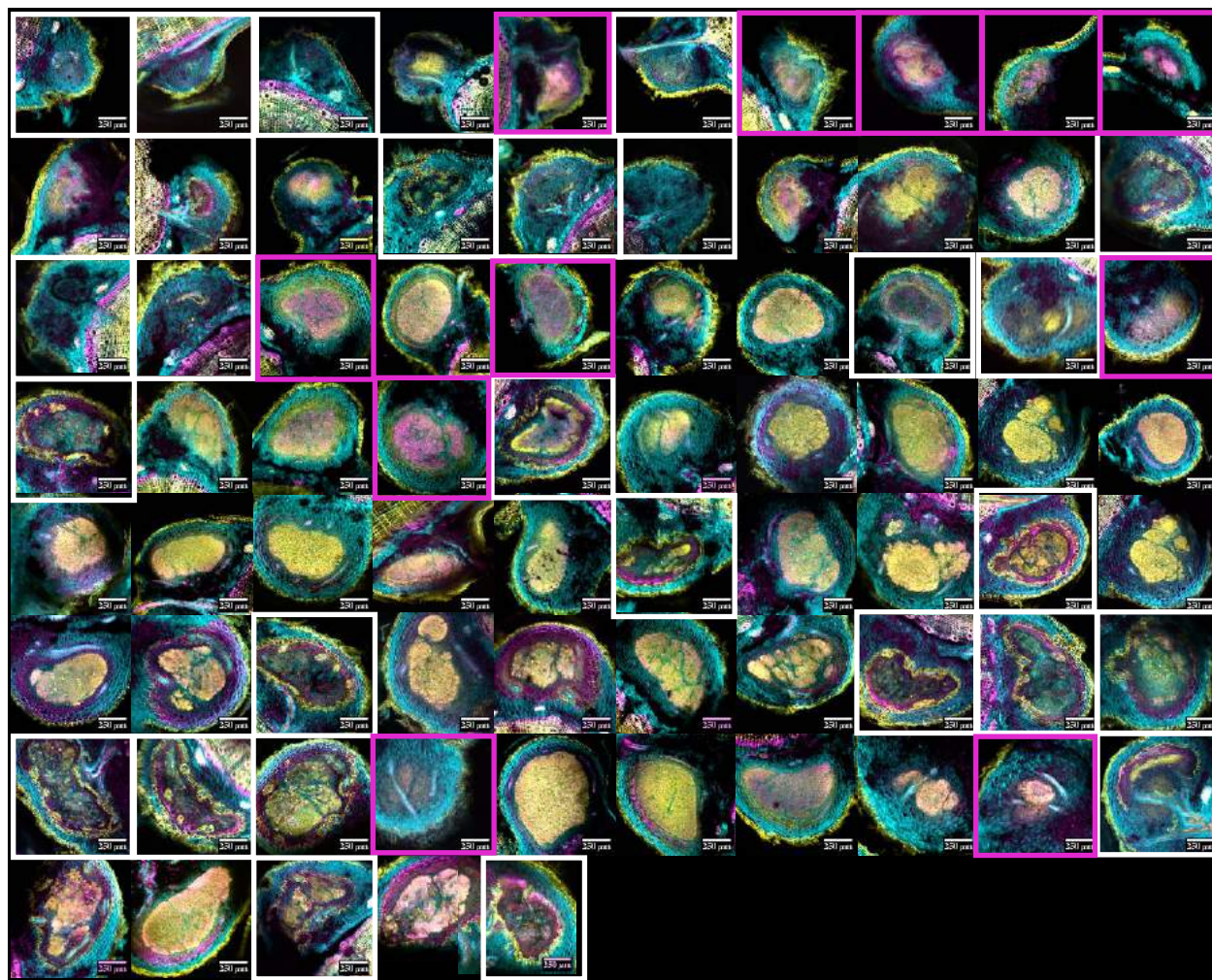
Figure 4-S1.

Figure 4-S2.

Figure 4-S3.
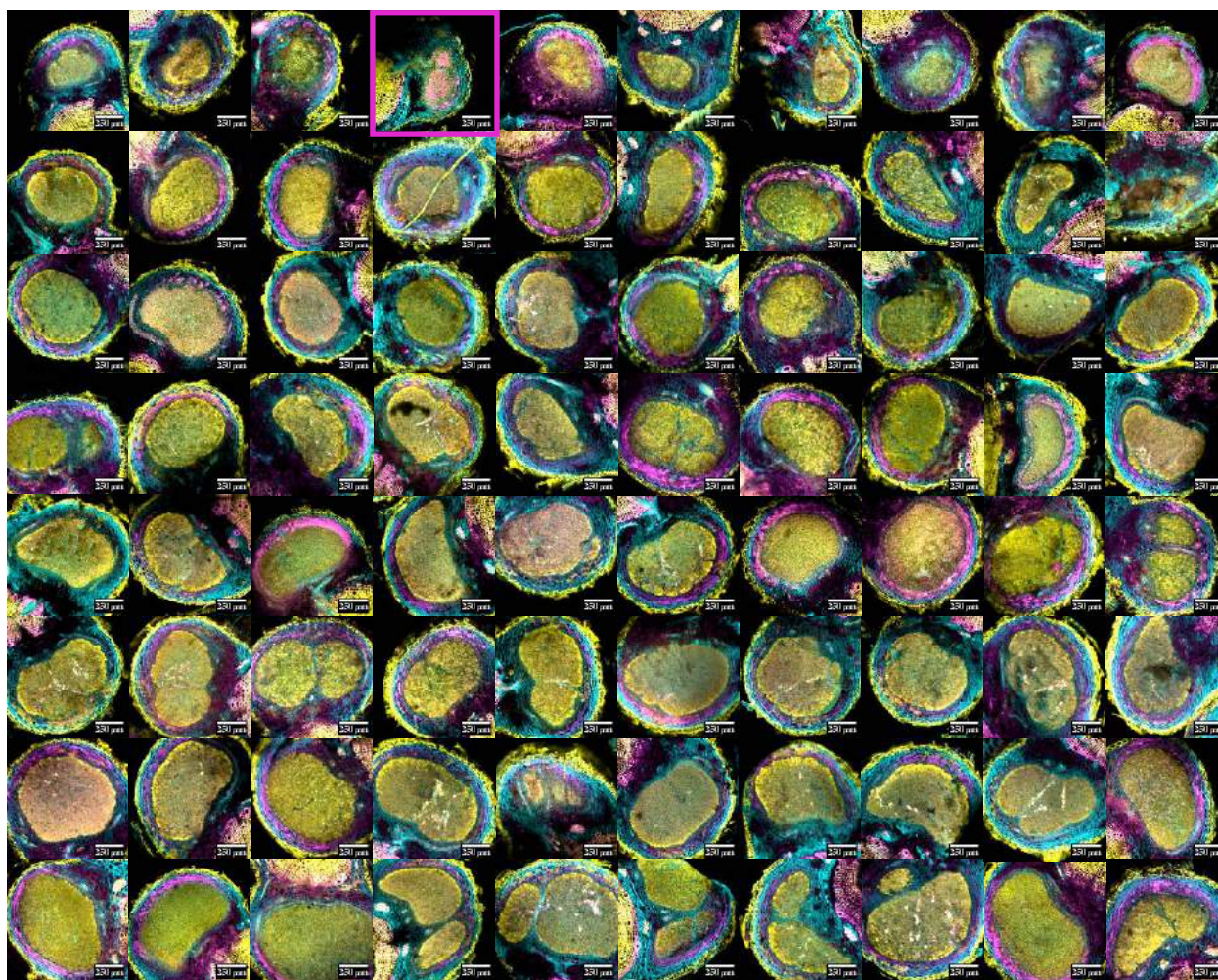
Figure 4-S4.
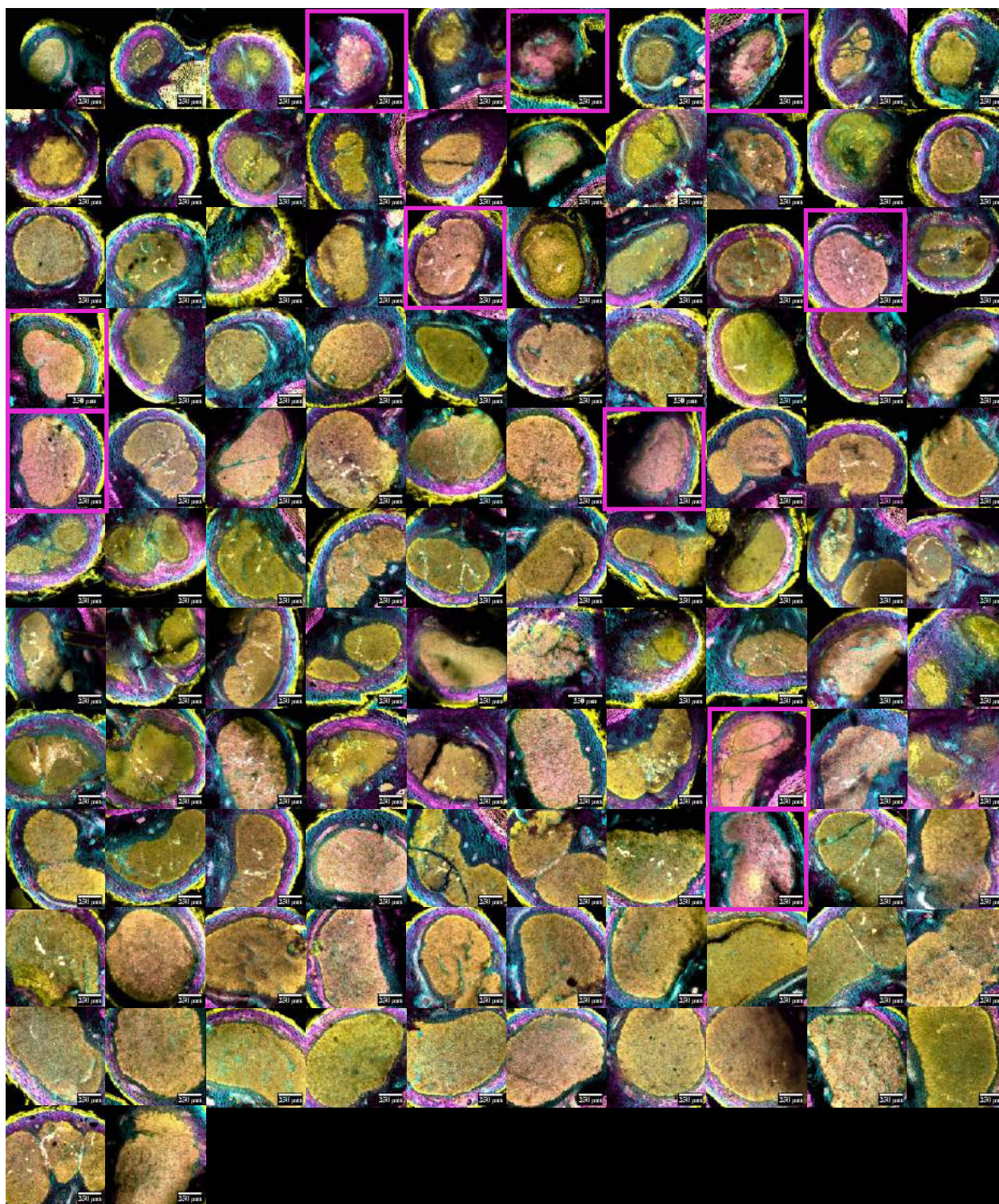
Figure 4-S5.
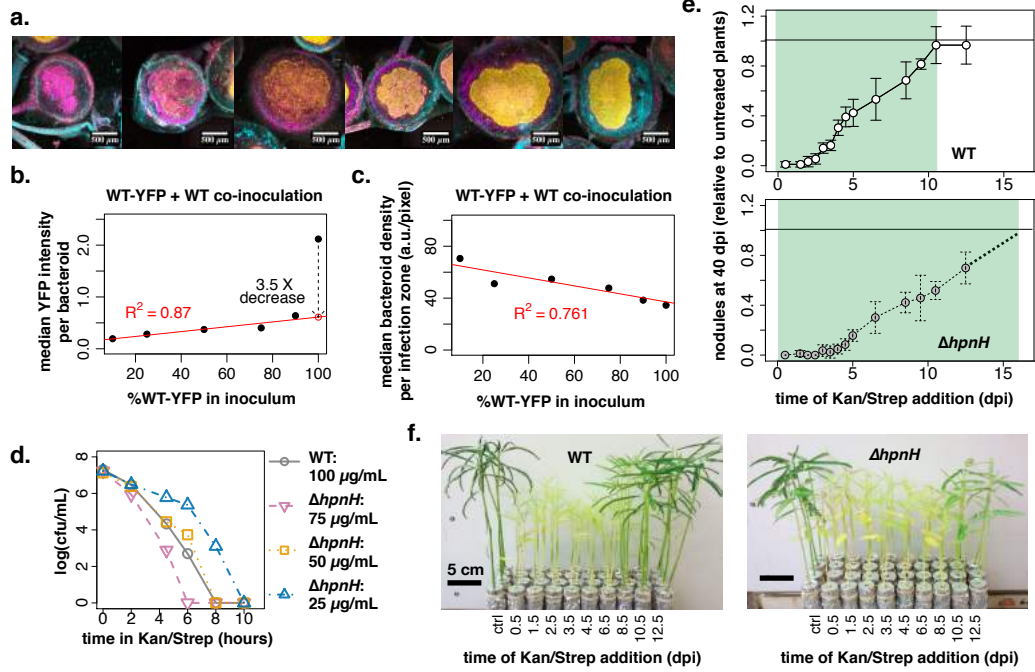
Figure 5.
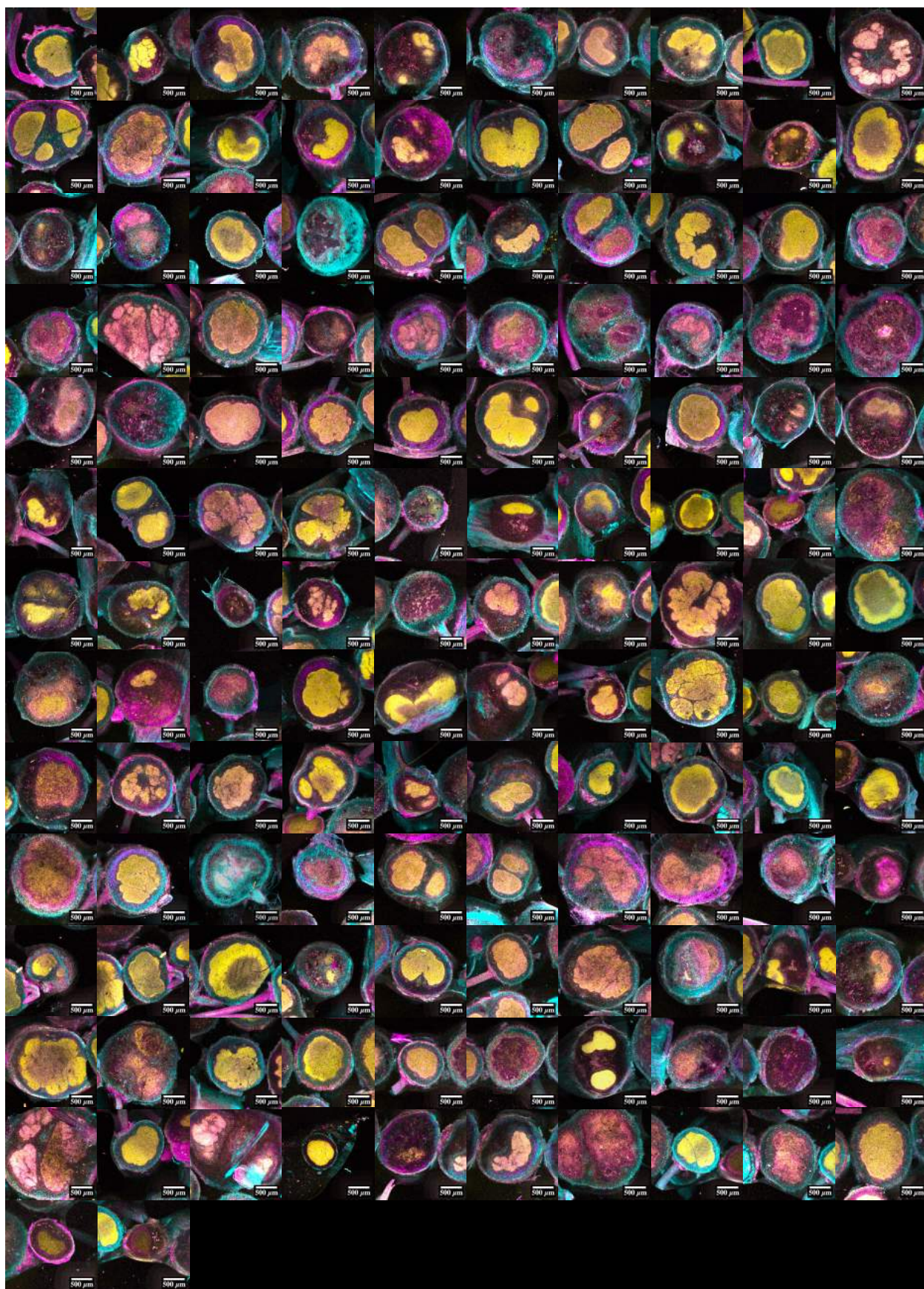
Figure 5-S1.
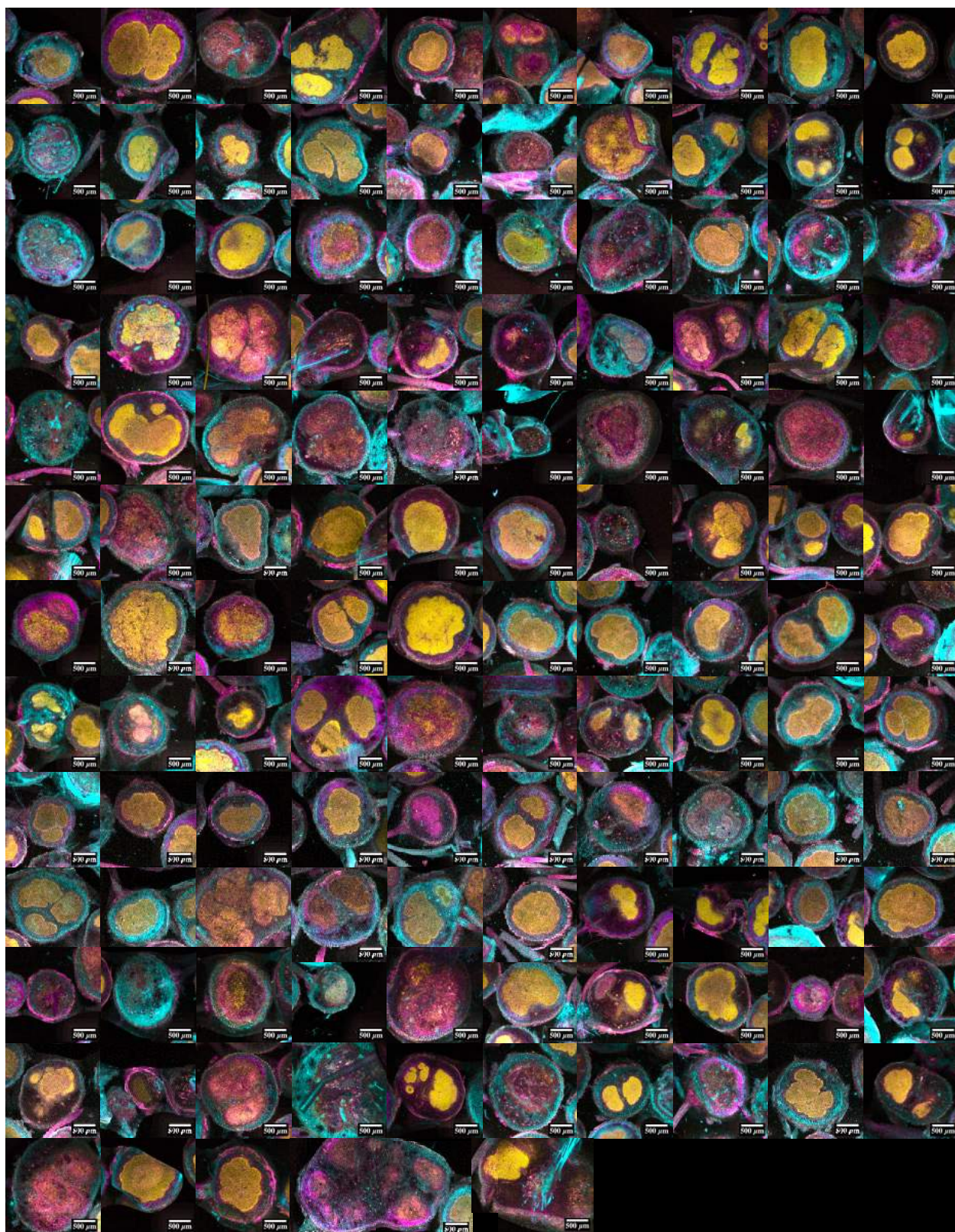
Figure 5-S2.
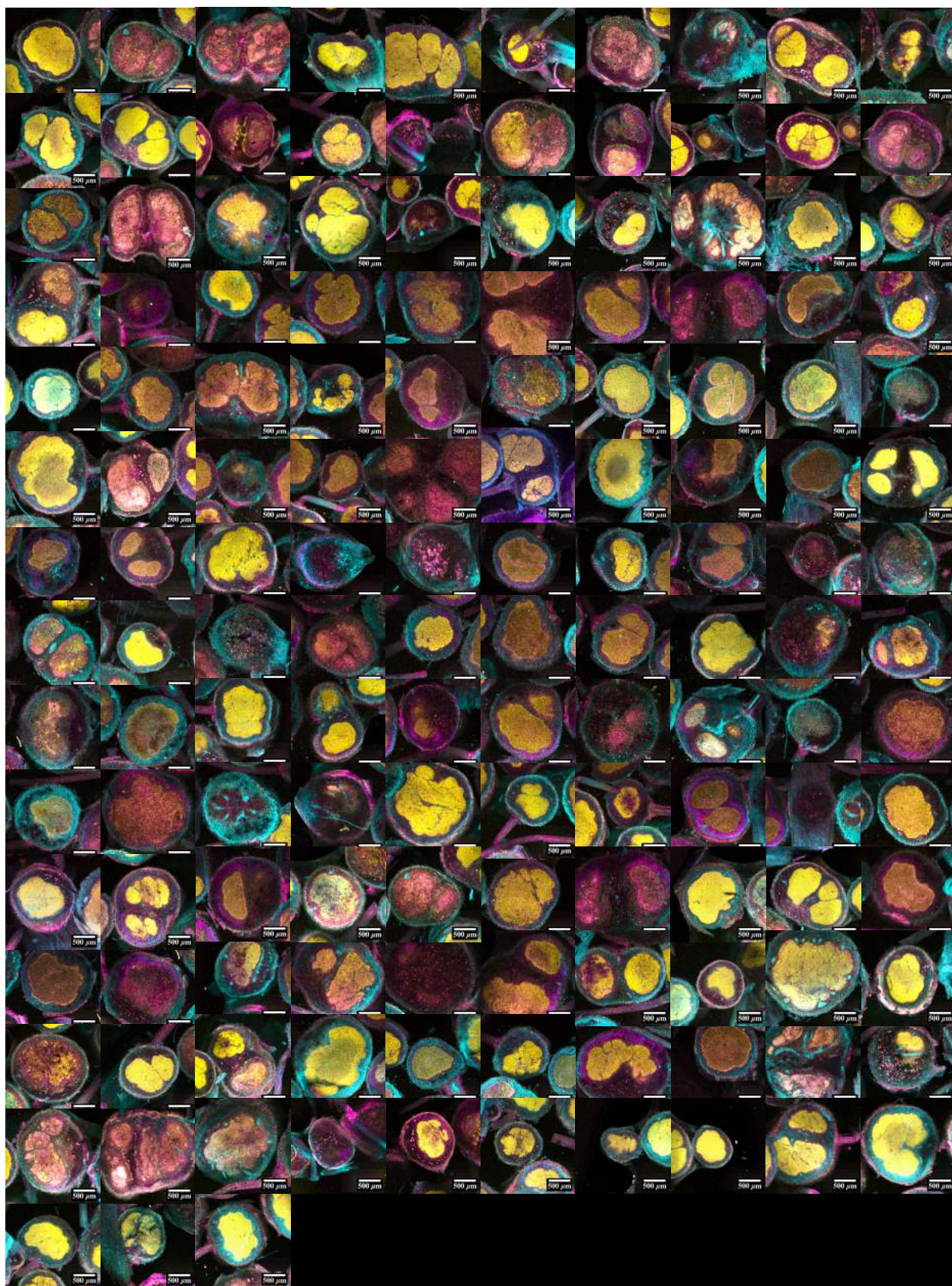
Figure 5-S3.
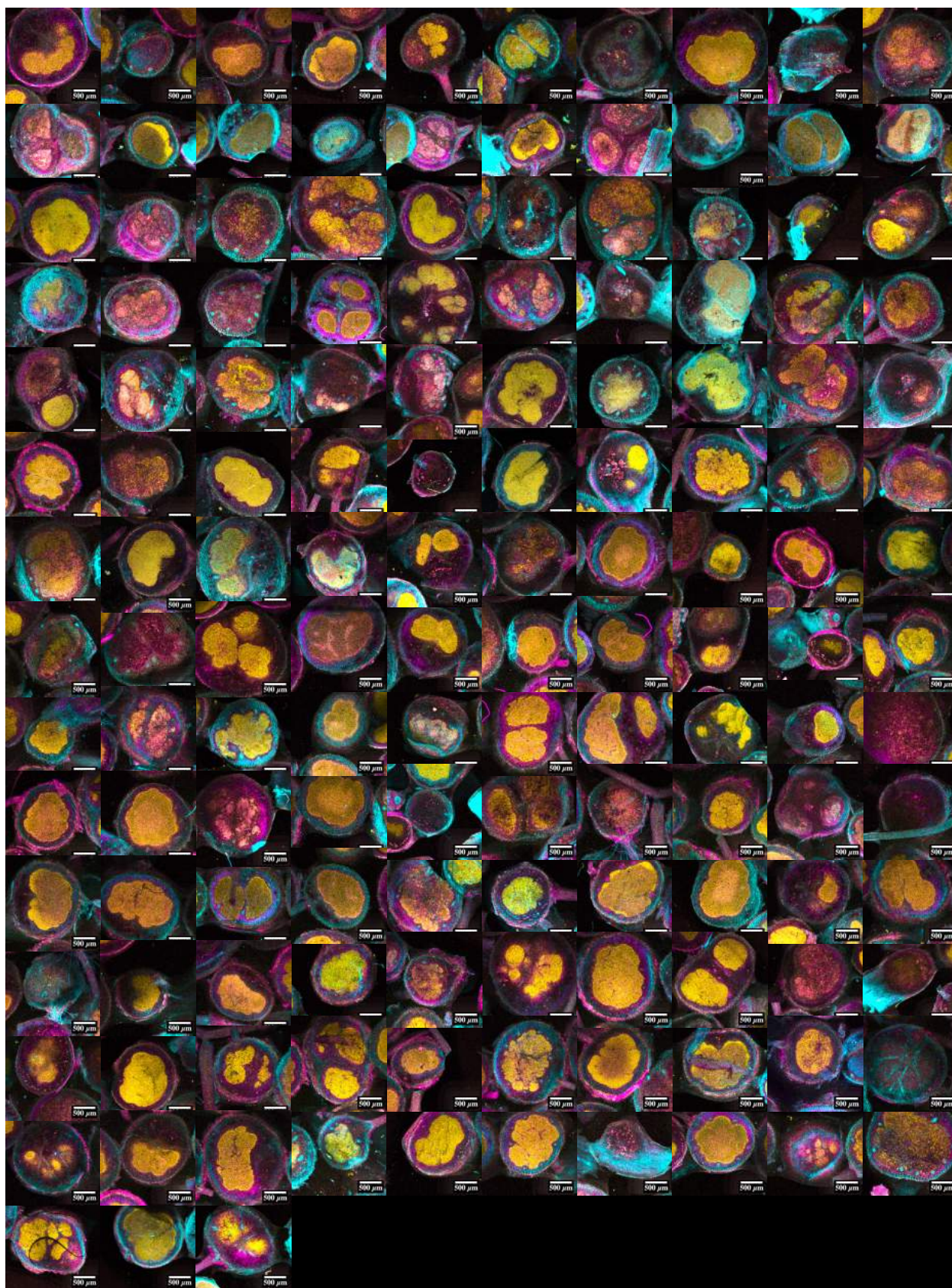
Figure 5-S4.
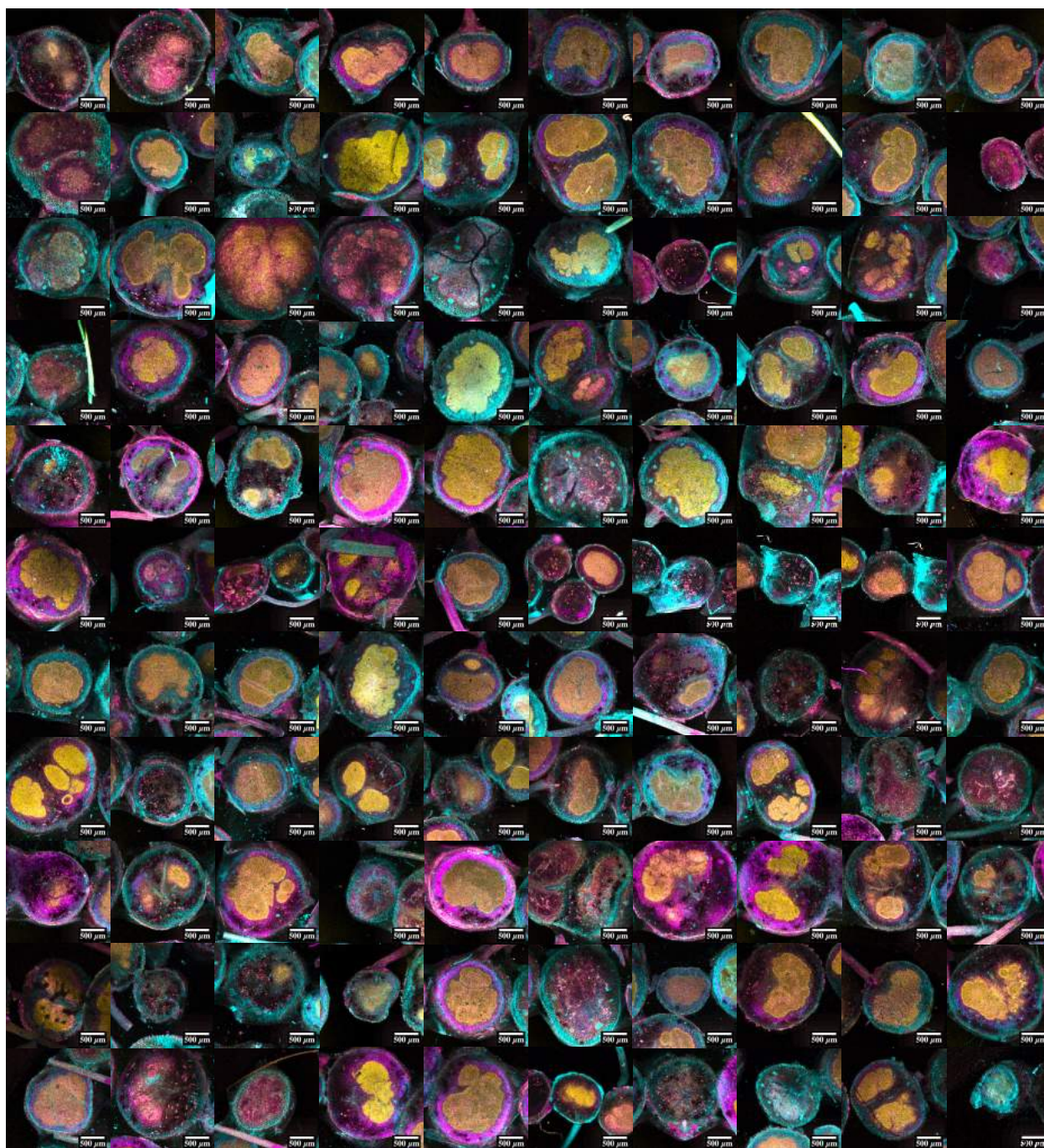
Figure 5-S5.
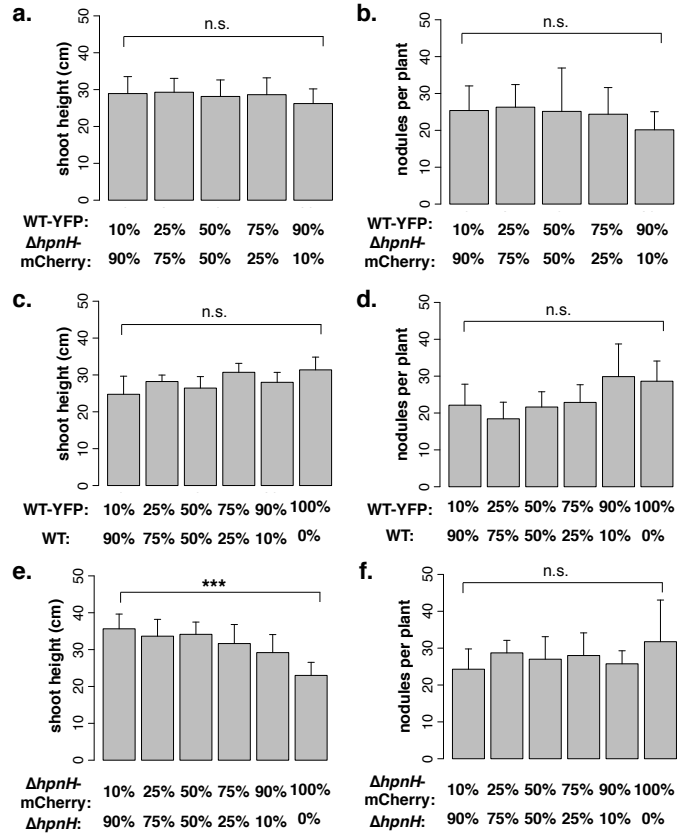
Figure 5-S6.
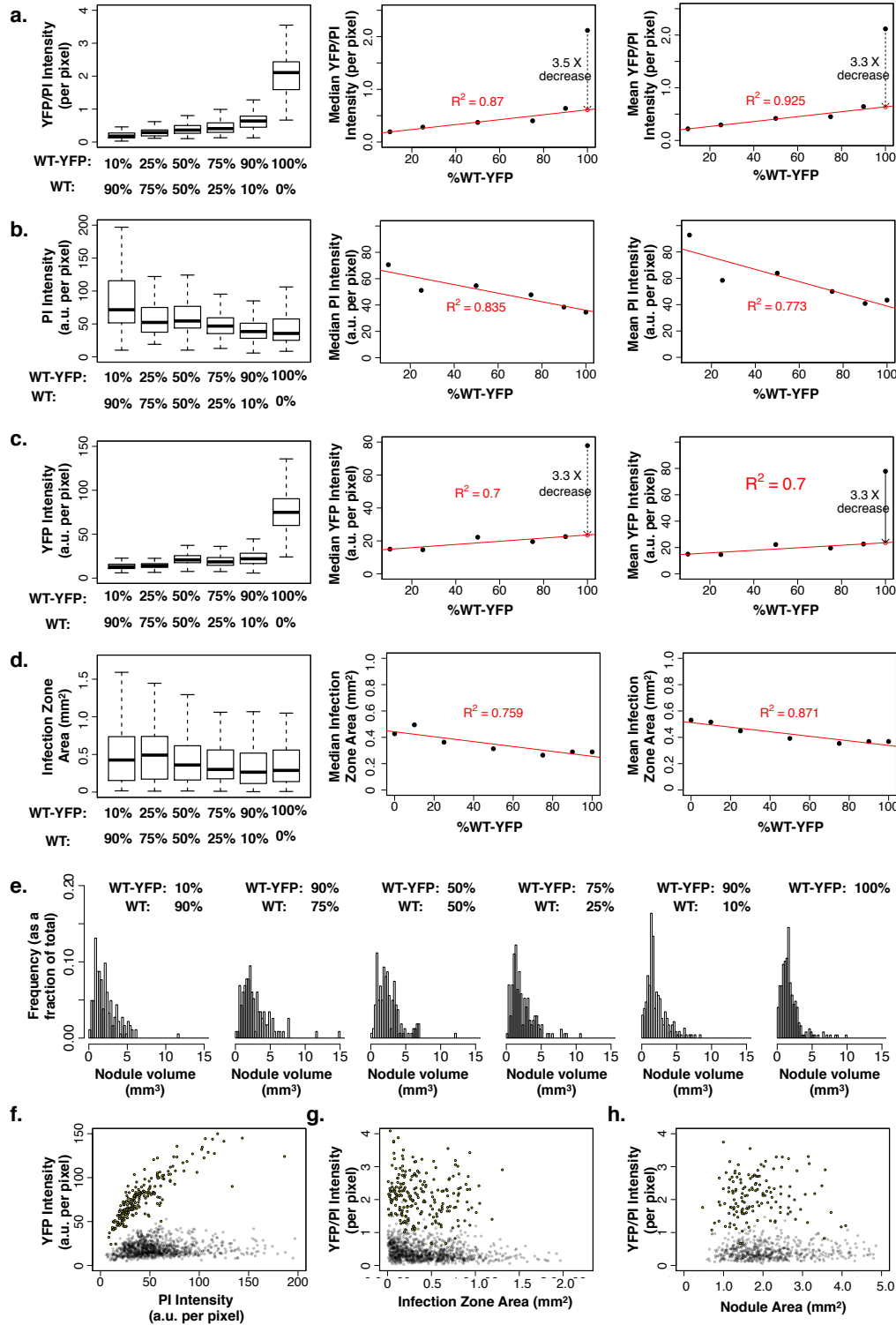
Figure 5-S7.
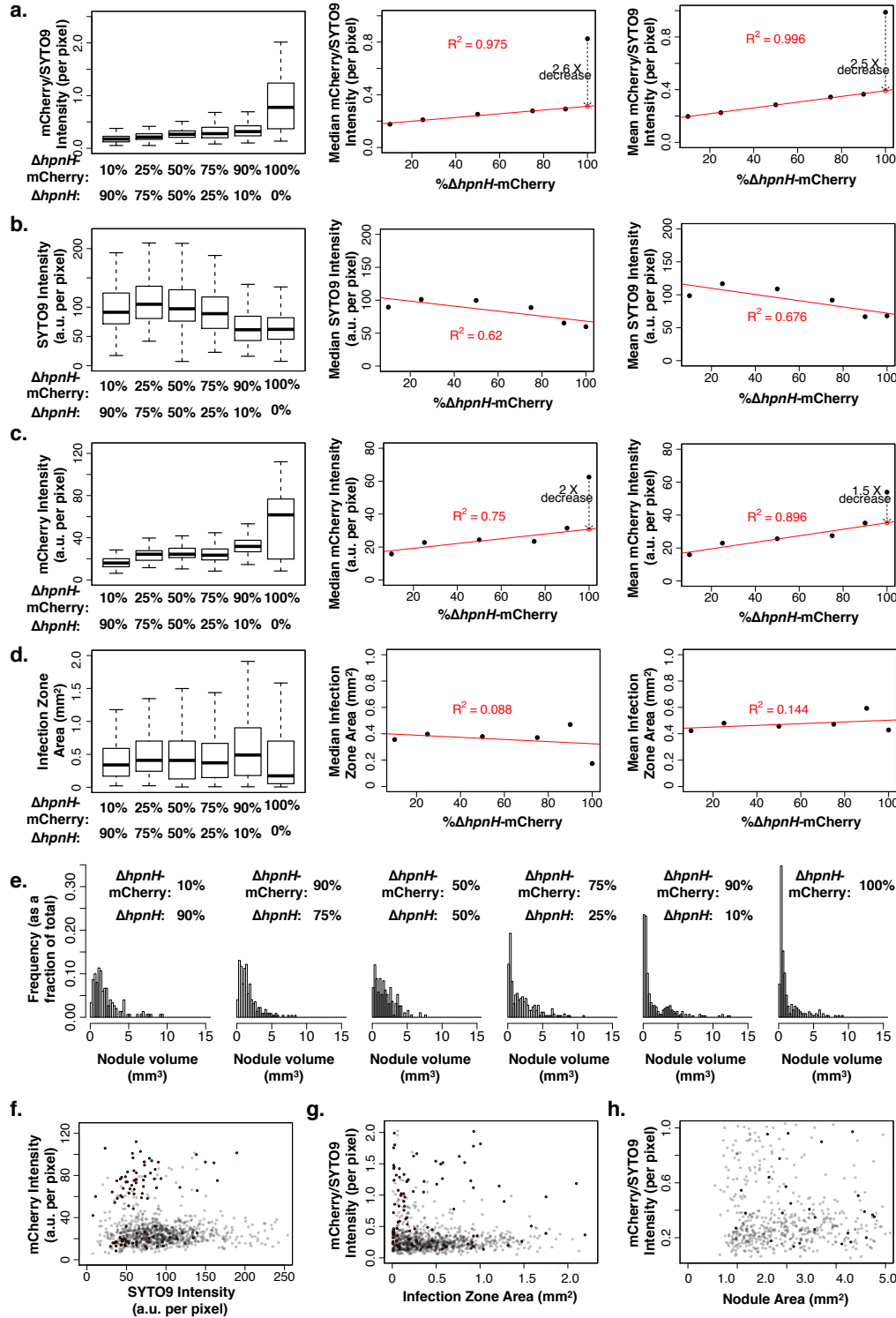
Figure 5-S8.
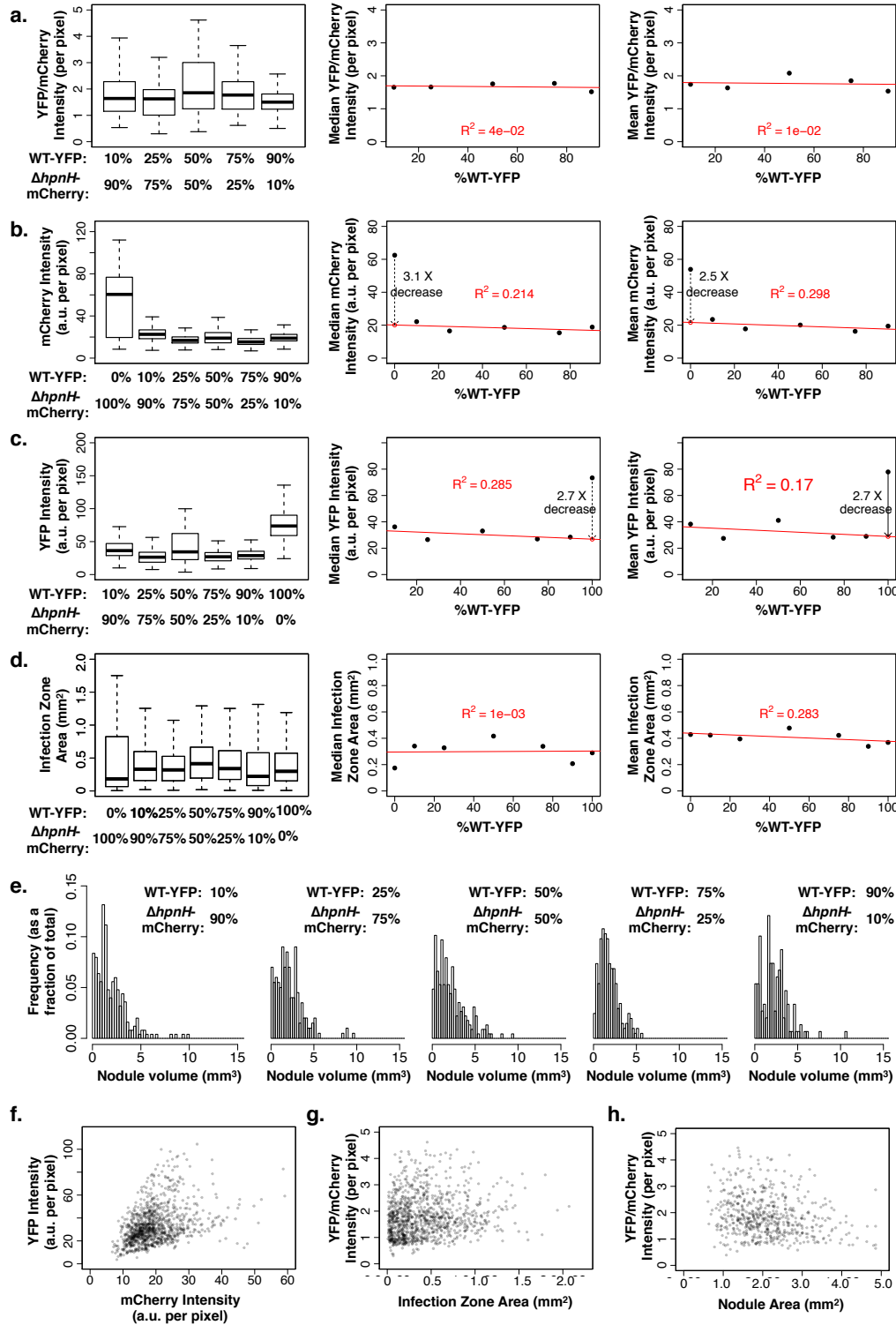
Figure 5-S9.
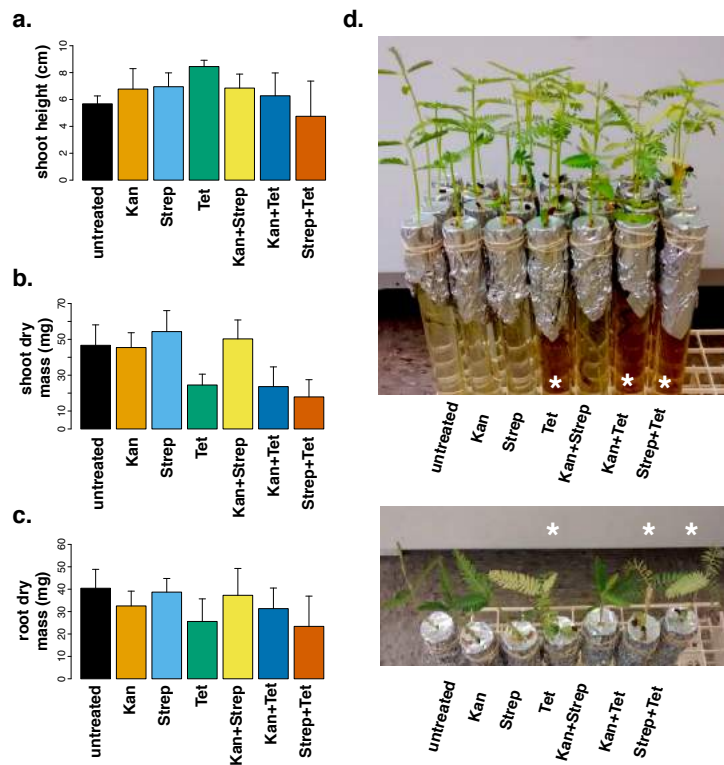
Figure 5-S10.
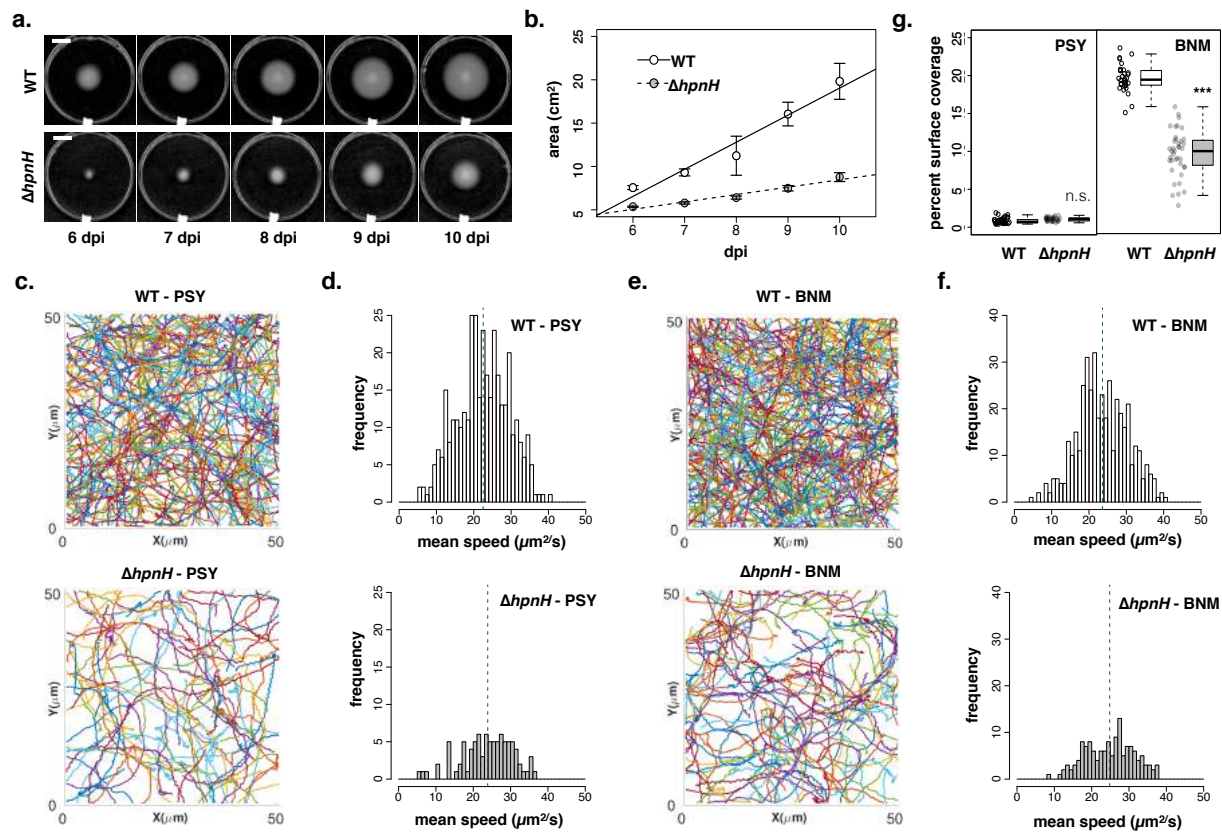
Figure 6.

Figure 6-S1.

Figure 7.